

Non-trivial dynamics in a model of glial membrane voltage driven by open potassium pores

Predrag Janjic¹✉, Dimitar Solev¹, Ljupco Kocarev¹

¹Laboratory for Complex Systems and Networks, Research Centre for Computer Science and Information Technologies, Macedonian Academy of Sciences and Arts, Skopje, North Macedonia

✉predrag.a.janjic@gmail.com

Abstract - Despite the molecular evidence that the nearly linear steady-state current-voltage relationship in mammalian astrocytes reflects a total current resulting from more than one differently regulated K^+ conductances, detailed ODE models of membrane voltage V_m are still lacking. Repeated experimental results of deregulated expressions of major K^+ channels in glia, Kir4.1, in models of neurodegenerative disease, as well as their altered rectification when assembling heteromeric Kir4.1/Kir5.1 channels have motivated us to attempt a detailed model incorporating the weaker potassium K2P-TREK1 current, in addition to Kir4.1, and study the stability of the resting state V_r . The main question is whether with a deregulated Kir conductivity the nominal resting state V_r remains stable, and the cell retains a trivial, *potassium electrode* behavior with V_m following E_K . The minimal 2-dimensional model near V_r showed that certain alterations of Kir4.1 current may result in multistability of V_m if the typically observed K^+ currents - Kir, K2P, and non-specific potassium leak are present. More specifically, a decrease or loss of outward Kir4.1 conductance (turning the channels into inwardly rectifying) introduces instability of V_r , near E_K . That happens through robustly observed fold bifurcation giving birth to a second, much more depolarized stable resting state $V_{dr} > -10$ mV. Realistic time series were used to perturb the membrane model, from recordings of glial V_m during electrographic seizures. Simulations of the perturbed system by constant currents through gap-junctions and transient seizure-like discharges as local field potentials led to depolarization of the astrocyte and switching of V_m between the two stable states, in a downstate – upstate manner. If the prolonged depolarizations near V_{dr} prove experimentally plausible, such catastrophic instability would impact all aspects of the glial function, from metabolic support to membrane transport and practically all neuromodulatory roles assigned to glia.

Statement of Significance – The almost linear current-voltage relationship of most glial membranes results from multiple non-linear potassium leaky-pore, or background conductances. The corresponding channel types develop and deregulate independently, some of them asymmetrically – deregulate differently in different V_m ranges. Effect of those deregulations on whole-cell voltage responses has not been treated. We developed a minimal ODE model of voltage dynamics incorporating detailed models of the different potassium currents based on electrophysiological recordings. Parametrically inducing some of the reported deregulations of Kir current in glia resulted in instability of the nominal resting membrane potential and appearance of a second much more depolarized resting state. If prolonged glial depolarizations prove plausible such bistability would change the present beliefs about glial V_m dynamics.

1. Introduction

Membrane voltage control in glia - The temporal dynamics of membrane voltage (V_m) of glial cells, the non-excitable neural cells, is a difficult subject to treat due to their structure-function complexity, and the experimental limitations to precisely measure V_m of their leaky membrane by the standard electrophysiological methods [1]. The classical, more than 50 years old view of the glial membrane as a *passive potassium electrode* [2] reflected the early observations that K^+ conductances in astrocytes accounting for the major part of ion conductivity near the resting voltage are of Ohmic nature. It is important to note that those early observations, lacking molecular specificity, have come from studies with a rather narrow experimental focus on the glial role in ion homeostasis, i.e., in the removal of the excess extracellular K^+ following sustained neuronal firing. Intensive molecular studies in the last twenty years seriously challenged the view of purely passive electrochemical response capability of glia, upon evidence that their membrane voltage V_m is transiently perturbed by different electrogenic pathways through transporters and ionotropic receptors [3], [4], expressed with certain variations by both neurons and glia. Today we know that

glial glutamate and GABA transporters, and even more intriguingly ionotropic glutamate and GABA receptors in some glia cell types [5], do alter glial V_m , [6] and therefore introduce forms of feedback control of their respective neuromodulatory functions. Such different control roles of glial V_m translate to a wide range of cellular and systemic functions from glucose transport and neurotransmitter recycling, via responses to mechanical and acidic stress, to the regulation of excitation-inhibition balance in local circuits.

Therefore, with the glial V_m playing both roles: a control variable (*controller*) of different neuromodulatory loops, as well as itself being a neuromodulatory target, the *dynamical stability of glial resting membrane voltage* V_r in response to various perturbations remains a central question in quantitative whole-cell modeling of glia. Such a dual effect of V_m as a variable, further qualifies the glial membrane as a *sensor and transducer of K^+ changes as a signal*, which perspective has been pushed by pioneers of glial biology [7] but further demands explanatory biophysical models.

The typical, transient perturbations of glial V_m comes either as: (i) transient variations of local field potential which directly polarize the membrane, (ii) varying trans-junctional voltage at the gap-junction connections of heavily interconnected astrocytic cells, or (iii) as transiently altered $[K^+]_o$. Prospective dynamical modeling studies would try to distinguish the specific, causal responses of glial V_m to a specific form of modulation, from the permanent stochastic electrochemical or other perturbations of V_m near the V_r .

Variations of V_m in a steady and perturbed glial membrane - Experimental studies of astrocytes *in situ*, the most abundant glial cell subtype in the brain, find that their V_m in nominal conditions fluctuates within a narrow range [8], [1]. From several millivolts, in response to nominal fluctuations of the local field, up to $10 \div 20$ mV more depolarized from V_r , in cases of seizures, other strong synchronous discharges in the neighboring neurons or spreading depolarizations accompanied by high, transiently elevated $[K^+]_o$ [9], [10], or [11] for review. Even though accumulated extracellular K^+ depolarizes glia, it is not clear how fast, and how closely glial V_m follows the perturbed E_K when both active and passive transport mechanisms switch in, and what is in turn the sign of the driving force $\Delta V_m = V_m - E_K$ that direct the leaky currents in sustained depolarizations. Typically, the reversal potential of the isolated macroscopic Kir and K2P currents is close, but slightly more positive to the Nernstian reversal potential of potassium, E_K , and closer to the cell resting voltage V_r , which is typically between -80 mV to -70 mV in glial cells, *in situ*. A relevant dynamical model of V_m would thus require incorporating the *minimal*, yet detailed description of the major glial ion conductances active near V_r , over several timescales from milliseconds to minutes, under assumption $[K^+]_o$ dynamics is not modeled, i.e., E_K remains a changeable parameter.

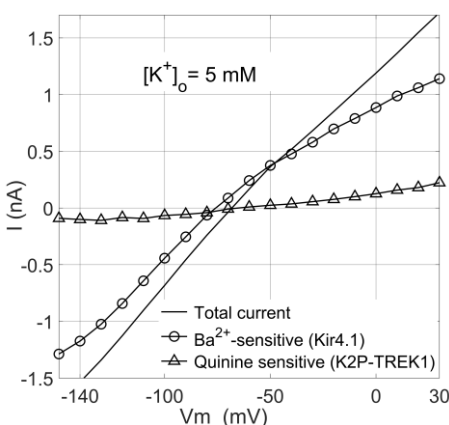


Figure 1 - Potassium current profile in isolated astrocytes – Kir4.1 current isolated as Ba^{2+} -sensitive, by application of 0.1mM BaCl (circles / line, N=9) reverses at $V_{rev} \approx 75.35$ mV, compared to the total K^+ current, black solid line (data from [12]). Of the remaining K^+ conductance, K2P current (max. 0.23 nA at +30mV), was isolated as quinine-sensitive, triangles / line. The transcript analysis of the K2P channels suggested a prevalence of K2P2.1 TREK1 isoform [12]. The sum of Kir4.1 and K2P2.1 current accounts for 82% of the total current at -120mV, and 80% at +30mV. Recordings from 9 cells, with a mean effective patch capacitance of 20 pF, have been normalized, averaged, and rescaled in the measured current range.

Figure 1 shows the steady-state current-voltage (I-V) recordings of the total K^+ current, as well as the isolated Kir4.1 and K2P-TREK1 currents in our data, obtained under whole-cell voltage-clamp protocol in $N = 9$ freshly isolated astrocytes from mouse hippocampus, bathed in slightly elevated extracellular $[K^+]_o = 5$ mM [12]. In steady-state conditions under a physiological K^+ concentration gradient, the barium Ba^{2+} - sensitive *weakly rectified* Kir4.1 current (circles) dominates the total current profile (solid line). Even though much weaker in resting conditions, the K2P current

(triangles) has different kinetics and electrochemical regulation, which requires to have it incorporated into any quantitation of K^+ conductivity in astroglia, either experimental or theoretical.

Describing these dominant K^+ background currents in isolated astrocytes from mouse hippocampus [12] together with a small K^+ leak current is the central modeling effort in this study. The isolated K^+ currents operate close to, and therefore define the resting membrane potential V_r in the proposed minimal ordinary differential equation (ODE) model of V_m dynamics. Apart of K^+ conductances, no other major conductances have been verified in astrocytes in the voltage range around V_r , assuming no osmolar stress which triggers non-negligible Cl^- transients. Co-expressed *Kir* and *K2P* channels account for the major fraction of potassium channels in almost all glial cells in the brain [13], cardiomyocytes and cardiac fibroblasts [14], [15], as well as in various cell types in renal epithelia [16], [17]. With over forty different channel isoforms in total, the co-occurrence of *Kir* and *K2P* channels in these, as well as in other tissues [18] is pervasive, resulting in different K^+ channel mix and therefore different I-V curves and kinetic properties of the total current.

Parametric analysis of the model reproducing some of the observed biological (de)regulation of those conductances suggests that astrocytic V_m could be prone to multistability in case of deregulation of the major weakly-rectified *Kir4.1* current (WR-*Kir*). Numerical simulations of the model perturbed using realistic recordings from glia *in-situ* [9], illustrated the bistability of the otherwise stable resting state. Although a mix of only K^+ conductances may give rise to two membrane resting states, already observed experimentally in cardiomyocytes [14], and described by a simple, generic minimal 2-dimensional conductance-based model [19], it has not been demonstrated so far in the glial membrane or simulated numerically using a glia-specific model.

2. Model of astroglial whole-cell V_m dynamics

Detailed electrophysiological studies of glial¹ conductances [12] are rare, and a widely accepted minimal dynamical model of V_m in astrocytes is therefore lacking. Further to the experimental complexity mentioned above, depending on the model system, sometimes additional regulation of these conductances by other environmental stimuli requires specific quantitation.

In what follows we outline the description of experimentally measured steady-state I-V relationships of *Kir4.1* and *K2P-TREK1* conductances. The nonexistence of a *voltage-sensing domain* - a structure present in other *gated* K^+ channels, suggests their rectification properties come from permeability regulation by physiological blocking ions, or by other Coulombic interactions on a pore level [20] resulting in voltage activation. The suggested modeling approaches to either *Kir* or *K2P* currents do not follow the Hodgkin-Huxley approach for gated channels but reflect their known biophysics as open pores. The proposed models could be applied *as-are* to a different mix of those channels in different cells or tissues. In the rest of the text, for the cell-specific aspects, without loss of generality, we restrict to an isolated hippocampal astrocyte as our model system [12].

2.1 Steady-state I-V model of weakly-rectified *Kir* current - Since the early quantitative studies, the conductivity of *Kir* channels under changing $[K^+]_o$, [21] indicate that *Kir* channels display voltage dependence on the electrochemical driving force $\Delta V_m = V_m - E_K$, rather than solely on the net membrane voltage V_m . This implies that proposed models should: (i) allow for variable $[K^+]_o$, and (ii) describe qualitative changes on different timescales, relevant not only for the millisecond V_m dynamics, but for the slower $[K^+]_o$ variations spanning from hundreds of milliseconds to seconds and minutes, as well.

Our central modeling proposition is a detailed description of the I-V relationship of the *weakly-rectifying* potassium *Kir* current (WR-*Kir*), rather than straightforwardly assigning the Hagiwara model of strongly inwardly-rectifying channels in egg cells [21]. The Hagiwara model is usually chosen under the assumption that V_m is very tightly regulated round the negative resting potential of $V_r \approx -80mV$, which is oversimplification because astrocytic V_m is exposed to perturbations that

¹ In the rest of the text, we will interchangeably use the terms *glia*, *astroglia* or *astrocytes* for the population of the astrocytic cells. Where reference is made to other glial cell types, those are named specifically.

significantly depolarize the cell into a V_m range where the curves of inwardly and weakly rectified Kir current markedly differ. To fill this gap requires describing quantitatively the outward conductivity of WR-Kir channels, which represent a comparable fraction to the inward component, Fig. 1 (circles).

The key assumption is that the steady-state WR-Kir current, Fig. 1 (circles), could be *dissected into two additive components*: a) inwardly rectified Kir component I_{Kir} , and b) outwardly rectified, or *residual Kir component* I_{res} , so that for the total isolated Ba^{2+} -sensitive Kir4.1 current we can write:

$$I_{Kir} = I_{inw} + I_{res} \quad (nA). \quad (1)$$

The two unidirectional fluxes result from a different manifestation of a *voltage-dependent block* of the pore by polyvalent cation which in turn result in different outward and inward permeation. Structure-function studies of Kir channels have shown a large extent of molecular similarity between the strongly and weakly rectifying channels, where a single point mutation dominantly impacts unidirectional permeation in open pores [22], [23]. We describe the permeation on a *short-pore model* of K^+ pore, formulated using a simplified one-dimensional reaction coordinate. It is generic for all K^+ open pores, where the cytoplasmic domain of the channel is ignored as not critical for describing the permeation, Fig. A1. See *Appendix 1* for a detailed description of the short-pore and further biophysical reasoning on the legitimacy of modeling two separate, additive fluxes in the weakly rectifying Kir pore, see *Appendix-1*. In the rest of the text charge will be represented in molar units of F , (C/mol) and the energy in the energy profiles will be normalized by $RT = 0.593 \text{ kcal/mol}$ at $T = 298 \text{ K}$ accordingly and expressed in *RT units*.

Inwardly rectified WR-Kir flux results from a negative driving force, $\Delta V_m < 0$, where the blocking ions, Mg^{2+} or other polyvalent cations are kept within the water cavity (Fig.A1.B) of the short-pore by Coulombic forces of the negative residues of transmembrane helices (Fig. A1.A). Such ion-crowding of permeant and blocking ions (Fig. A1.B) results in an inward pseudo gating of the WR-Kir pore producing an equilibrium probability of open, inwardly conducting pore described by Boltzmann term, as originally introduced by the Hagiwara model [21]:

$$I_{inw} = g_{Kir-inw}(V_m - E_{Kir}) \quad (nA) \quad (2)$$

$$g_{Kir-inw}(\Delta V_m) = \frac{A \bar{g}_{s-inw} \sqrt{[K]_o}}{1 + \exp(-z_{inw}(\Delta V_m - \Delta V_{12})/v_s)} \quad (\mu S) \quad (3)$$

$$\Delta V_m = (V_m - E_{Kir}), \quad \Delta V_{12-inw} = (V_{12-inw} - E_{Kir}) \quad (mV),$$

where \bar{g}_{s-inw} represents the maximal value of the $g_{Kir-inw}$ obtained as a slope of the linear segment in the recorded I/V curve negative of E_K , V_{12-inw} is the voltage at half-maximal conductance, z_{inw} represents the effective charge valence of permeant ions in the short-pore, $E_{Kir} = -76 \text{ mV}$ is the reversal voltage of the isolated Kir4.1 current, and $A = 1.0 \text{ mM}^{-1/2}$ keeps the conductance of μS . Figure 2A, the solid black curve, shows a fitted sigmoid function, Eq. 3, to numerically differentiated Kir4.1 I-V data, from Fig. 1 (blue curve, for $[K^+]_o = 5\text{mM}$), for V_m more negative than E_{Kir} . Such numerically obtained series physically represents a slope conductance, whereas the values more negative to -110mV (blue crosses) are discarded due to slope deviation (Fig.1) originating from a known effect of voltage-dependent pore block by external Na^+ ions [24], [25]. The fitting gave $A \cdot \bar{g}_{s-inw} \sqrt{[K]_o} = 20.6 \text{ nS}$, $V_{12-inw} = -53.5 \text{ mV}$ and $z_{inw} = 1.638$, producing the blue curve in Fig. 2B. The effective charge z_{inw} , was in accordance with published charge estimates for the voltage dependence of block by small ions, for a summary see [26]. The slope factor $v_s \equiv RT/F = 25.7 \text{ mV}$, corresponding to room temperature of $T = 298.13 \text{ K}$ is kept constant throughout the text.

Outwardly rectified Kir4.1 flux results from outward pseudo gating for a more positive driving force $V_m > -60\text{mV}$ (Fig. A1.C), where outwardly directed driving force pushes partly or fully dehydrated

blocking ion towards the entry of the selectivity filter (SF), see *Appendix 1*. Such electrostatic, flickering block modulates ion association to the pore and the outward permeation.

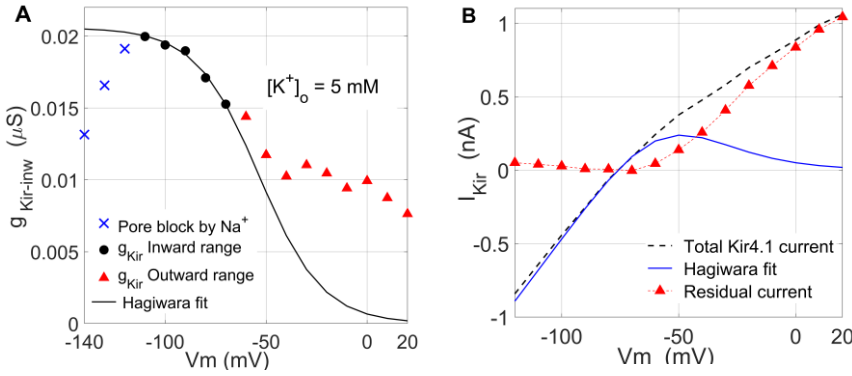


Figure 2- Separation of WR-Kir current in two unidirectional fluxes – (A) Fitting the conductance $g_{Kir-inw}$ by the Hagiwara model for $V_m \leq -60mV$, black line, with the crosses excluded. **(B)** The *residual outward* component, eq. (4), red triangles, obtained by subtracting the modeled inward current (blue), Eq. 2, from the total recorded Ba^{2+} sensitive Kir component (dashed line). Blue crosses in (A), and the small non-zero values carried over by the subtraction in (B) (red) for $V_m < -100 mV$, result from pore block by Na^+ .

To obtain numerical series for the residual, outward Kir4.1 current I_{res} (4) from the recordings, we subtracted the portion *described by the Hagiwara model* in the whole V_m range, Eq. 2 and Eq. 3, fitted near V_T , Fig.2B, blue line, from the total Kir current, red triangles in Fig.2B.

$$I_{res} = I_{Kir} - I_{inw} \quad (nA). \quad (4)$$

Non-constant field Goldman-Hodgkin-Katz (GHK) model of WR-Kir outward current - Without a voltage gate as a structural determinant of gating in Kir and K2P pores, other features like physiological block by cytoplasmic cations may produce pseudo gating by charge movement within the membrane or alter the Coulombic and/or structural forces defining open-pore permeability *within the single global state* of the channel.

We arrive at the proposed model of the residual current using the following assumptions:

- **GHK formalism without constant-field assumption** describes the outward conductivity, using Eq. 5 as a general form of GHK current equation before introducing the constant-field assumption [27], chapter 13.13. Instead, a simple, *quadratic potential energy profile* of an elastic force $U(x)$ introduces a parabolic energy barrier in the energy profile of an open Kir pore, Fig.3A, with the voltage drop over the pore added as linear, $V_m(x) = x\Delta V_m$. The U_{max} potential represents the peak of the *association* barrier to the permeant K^+ ion at the entry of hydrophobic SF in RT units. The barrier is centered at transition state x_T , while the positive w is the *force constant* of the elastic restoration force of Coulombic nature. For the charge in molar equivalents and the concentrations in $[mM]$, we will describe the outward current using:

$$I_{res} = zFD \frac{[K^+]_i - [K^+]_o e^{-\frac{zFV_m}{RT}}}{\int_a^b e^{U(x) - zFV_m(x)/RT} dx} \quad (nA), \quad (5)$$

$$U(x) = U_{max} - w(x - x_T)^2 \quad (RT \text{ units}).$$

We can extend the interval (a, b) to $(-\infty, +\infty)$ because the energy profile falls sharply outside the short pore. Depending on the description of $U_{max}(V_m)$ the location of x_T could change, resulting in an asymmetrical shape of the barrier, sketched in Fig. 3A, dashed line, compared to the symmetrical case in Fig. 3B (barrier not shown). Different positions of the transition state, $x_T = l_{sp}/2$ in Fig. 3A, and $x_T = l_{sp}/3$ in Fig. 3B simply illustrate different model assumptions for the barrier position.

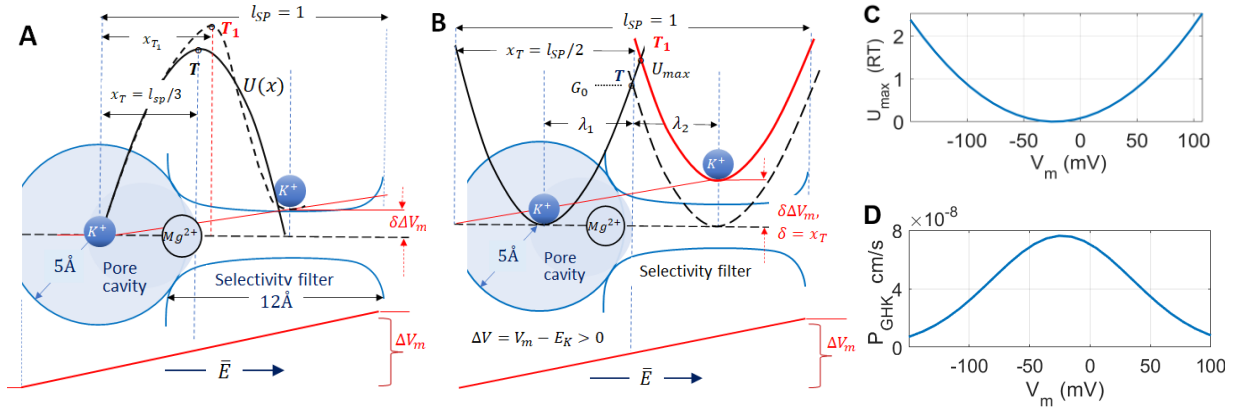


Figure 3 – Reaction coordinate in the model of WR-Kir outward permeation – (A) Quadratic energy barrier profile centered at the transition state x_T used in Goldman-Godgkin-Katz description of the outward flux of Kir4.1 current. Here the reaction coordinate starts at the center of the cavity, and the δV_m fraction of the voltage drops over the reaction coordinate, with a full length $l_{SP} = 1$. **(B)** Sketch of the Marcus free energy formalism defining voltage-dependence of x_T and the barrier height U_{max} . Voltage-dependent shift of $x_T(V_m)$ from T to T_1 and the selection of λ_1 and λ_2 positions of the energy wells in (B) produce either a symmetric (solid line) or skewed barrier at the top (dashed line) in (A). Here, compared to (A), the reaction coordinate spreads over the whole short-pore, and $x_T = 1/2$ places the peak of the symmetrical barrier at the entry of SF. **(C)** and **(D)** peak behavior of U_{max} , Eq. 7, and non-constant GHK permeability (9) at $V_C = -23$ mV which will produce maximal outward current I_{res} . The peak of P_{GHK} in (D) suggests the facilitating Coulombic effect of a polyvalent blocker on the outward permeation is maximal at V_C above which it gradually turns into full pore occlusion.

- Partial voltage-dependent pore occlusion by cytoplasmic cations activates the pore in the outward direction** – In this model voltage-driven localization of polyvalent cytoplasmic cations in the cavity produces a partial, flickering pore occlusion, Fig. 3A, which increases the Coulombic repulsion on the permeant ion associated with the SF. Such partial blocking serves as a plausible modulatory mechanism, with the pore remaining in a single open conformation. Therefore, both, the pseudo-gating on pore-level and the macroscopic current rectification are attributed to the voltage dependence of the block. This defines a voltage-dependent probability of an activated pore with an *effective, equivalent charge* $z_B > 1$, reflecting the valence of the blocking ion (Mg^{2+} or positively charged polyamines), not necessarily implicating a multi-ion pore. We illustrate this blocking configuration along the reaction coordinate of the short-pore model on the sketch in Figure A1.C, as a displacement of the blocking Mg^{2+} ion from S6 (center of the cavity) towards the S5 ion coordination site (SF entrance). To formulate the modulatory effect of blocking as a probability of *outward activation* in a non-gated channel, we use the Boltzmann equation in a classical way [27], chapter 1.12:

$$p_{out} = \frac{1}{1 + e^{-z_B(V_m - V_{12-out})/v_s}} \quad (6)$$

Since both, the Hagiwara model of Kir, as well as more recent permeation studies on K2P channels [28], suggested electro-chemical gating in K^+ pores, with effective driving force $\Delta V_m = V_m - E_K$, applying it within Boltzmann equation cancels out the reversal potential E_K in Eq. 6, as it also appears in the half-activation voltage $\Delta V_{12-out} = V_{12-out} - E_K$ (same as in Eq. 3). The slope factor v_s is the same defined within the model for inward flux.

- Quadratic dependence of barrier peak U_{max} on voltage saturates the outward flux** - We are adding nonlinear dependence of Marcus form, Eq. 7, to introduce a simple form of Coulombic contribution of the voltage-dependent block in U_{max} according to [27], see chapters 7.6 and 7.8:

$$U_{max}(V_m) = G_0(\lambda - x_T)^2 = G_0 \left(\lambda - \frac{z_B \delta(V_m - E_K)}{4\lambda v_s G_0} \right)^2; \quad \lambda_1 = \lambda_2 \equiv \lambda, \quad (RT \text{ units}), \quad (7)$$

which can describe the *saturation of outward flux* for very positive applied voltages, Fig.4. Figure 3B shows qualitatively the geometry of the Marcus energy landscape and $U_{max}(V_m)$ over a simplified, one-dimensional reaction coordinate. The peak of the barrier U_{max} at the intersection of the two parabolic wells, $2\lambda_1$ and $2\lambda_2$ wide, defines the transition state x_T . It separates the left energy well where the permeant ion dwells before the outwardly directed field drives it to the SF and the right well where the ion is associated to the pore. The critical parameter influencing U_{max} voltage dependence is the fraction of the linear voltage drop $\delta = 1/2$ that falls under the energy profile, reducing it to $\delta\Delta V_m^2$. Figure 3C illustrates the quadratic profile of $U_{max}(V_m)$ with the minimum attained at a critical voltage $V_C = -23\text{ mV}$. The nonlinear $U_{max}(V_m)$ dependence is significant for capturing the outward WR-Kir current saturation with voltage [29], [30], [20] which is not possible with a constant or linearly dependent U_{max} . The prefactor G_0 in RT units represents the height of the constant barrier due to hydrophobic repulsion in the absence of electrochemical driving force.

Equation 7 is based on the Marcus chemical kinetics theory describing the charge transfer in chemical bonding, using reaction rate models [31], which has meanwhile gained a wider acceptance in treating quasi-equilibrium changes in proteins, for review see [32]. We stress that we use here qualitative features of very simplified one-dimensional reaction coordinate in the Marcus theory, *to describe* macroscopic properties, like the saturation in the voltage dependence of block in measurements of macroscopic whole-cell currents, rather than to construct a model for predicting permeation rates or estimating the microscopic parameters of the pore, like z_B or G_0 [33].

Under the above assumptions, by solving the Gaussian integral in the nominator of Eq. 5 and simplifying the solution by setting a fixed position $x_T = 1/2$ [27], for the outward residual component I_{res} of isolated Kir4.1 current we obtain:

$$I_{res} = p_{out} zFP_{GHK} \left([K^+]_i e^{\frac{zV_m}{2v_s}} - [K^+]_o e^{-\frac{zV_m}{2v_s}} \right) \quad (nA). \quad (8)$$

$x_T = 1/2$ places the transition state and U_{max} at the entry of the SF where the blocking ion should be localized for positive ΔV_m , which is close to 1/2 of the length of the short pore with the cavity approximately 10\AA in diameter, and the SF length typically approximated to $12 \div 15\text{\AA}$, depending on the structure-function assumptions. The simplification removes $x_T(\Delta V_m)$ shift which if present, for illustration, for $\Delta V_m = v_s$, $\lambda_1 = \lambda_2 = 1/4$, with $z_B = 1.6$ and $G_0 = 6.6\text{ RT}$ obtained by fitting Eq. 8 to the series obtained by Eq. 4, shifts x_T from 0.5 to 0.56.

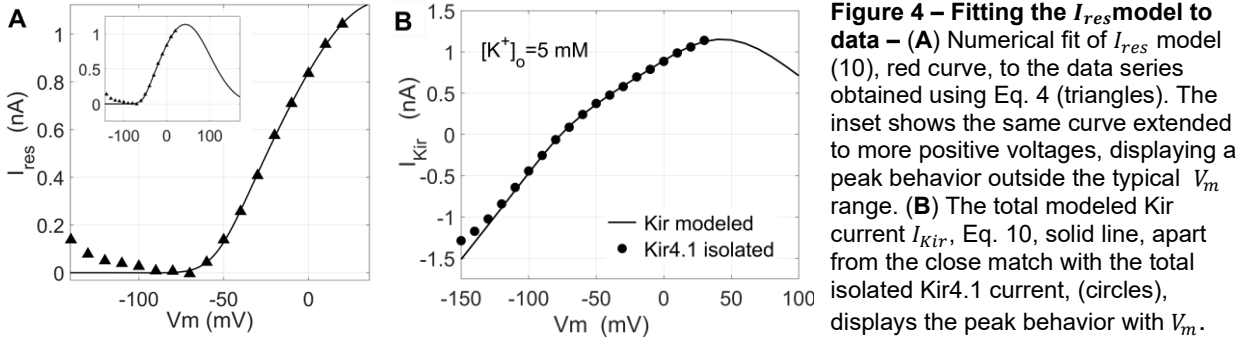
Having departed from the classical Nernst-Planck assumptions in solving Eq. 5 for a macroscopic description of I_{res} , by using Eq. 7 to add modulation of permeability by voltage-dependent block, P_{GHK} introduced in Eq. 8 absorbs the resulting prefactors and implicitly defines voltage-dependent permeability [27]:

$$P_{GHK}(V_m) = \sqrt{\frac{w}{\pi RT}} D e^{-\frac{U_{max}(V_m)}{RT}} = P_K e^{-\frac{U_{max}(V_m)}{RT}} \quad (cm/s). \quad (9)$$

Here w is the same force factor from the harmonic potential $U(x)$ in (5), and D is the classical, constant diffusion coefficient, both absorbed within the constant, voltage-independent K^+ permeability P_K multiplied by a factor of Arrhenius activation form with voltage-dependent barrier $U_{max}(V_m)$ introduced in Eq. 8. The zero RT minimum of $U_{max}(V_C)$, Fig. 3C, should be interpreted as a zero of the *voltage-dependent potential energy profile* at which we observe the maximal permeability P_{GHK} reducing to the constant value of $P_K = 7.63 \times 10^{-8}\text{ cm/s}$ in Nernst-Planck electrodiffusion, Eq. 9, Fig. 3D. The estimate is within the same order of magnitude as the ranges in the early studies of rectification in potassium channels, see [34] for a review. For references where

² δ represents a dimensionless fraction of the length of the pore $0 \geq \delta \geq l_{SP} \equiv 1$, or the “electrical” length of the pore.

explicit nonlinear dependence of GHK permeability has been used, mostly in models of neuronal calcium channels, see [35].



For the final form of the Kir current model to fit the isolated Kir4.1 current recordings, we get:

$$I_{Kir} = I_{inw} + I_{res} \quad (nA)$$

$$I_{inw} = g_{Kir}(V_m - E_K) = \frac{A \bar{g}_{s-inw} \sqrt{[K^+]_o}}{1 + e^{-z_{inw}(V_m - V_{12})/v_s}} (V_m - E_K) \quad (nA) \quad (10)$$

$$I_{res} = p_{out} z F P_K e^{-U_{max}/RT} \left([K^+]_i e^{\frac{zV_m}{2v_s}} - [K^+]_o e^{-\frac{zV_m}{2v_s}} \right) \quad (nA).$$

Fitting I_{res} model (10) with U_{max} given by Eq. 7 to the residual outward current data obtained by Eq. 4, using nonlinear least-squares error, gives the I-V graph in Figure 4A. The peak behavior in Eq. 7 produces a peak behavior of I_{res} in a more positive, non-physiological V_m range for glia, Fig. 4B. Such shape has already been reported in a study of a whole rodent hippocampus [29], with the curve shifted to more negative voltages.

All the parameter values, the fixed ones, and those obtained by fitting are listed in Table 1. The table values of I_{res} fitting parameters: P_K , V_{12-out} , G_0 , z_B , and z , to be later used in the parameter analysis of the model, were obtained as averages of ten curve fitting attempts with one of them varied within $\pm 10\%$ of the initial value in each run while the other four were recalculated by the NLSQ curve fitting. The blocking ion charge valence was bounded within $1.5 \leq z_B \leq 2.0$. The goodness of fit $R^2 \geq 0.98$ was achieved in all attempts.

2.2 Steady-state I-V model of K2P-TREK1 current – Studies isolating the weaker astrocytic currents after isolating Kir currents are rare, due to experimental issues with leaky astrocytic membrane, and therefore K2P currents are rarely quantified [12], [36]. Figure 5A shows pharmacologically isolated K2P current, using *quinine*, at $[K^+]_o = 5 \text{ mM}$ (black circles), as well as at drastically elevated external potassium at $[K^+]_o = 50 \text{ mM}$ (blue dots) in our recordings from [12]. Both I-V recordings were fitted (solid lines) with the standard GHK current equation [37], even though the permeation studies suggest multi-ion occupancy of the pore and some form of pseudo-gating [28]. Adding a small Na^+ permeability [37], $P_{Na}/P_K = 0.06$, within nominally non-conductive range (below -50 mV) improves the fit at 5 mM , Fig. 5A, dotted line. That effect of Na^+ on passive K^+ conductivity in glia is known [38], but we didn't use the correction within the numerical simulations due to a lack of recordings to verify P_{Na}/P_K ratio for notably elevated $[K^+]_o$ above 5 mM .

The K2P currents in this study [12] originate primarily from the K2P-TREK1 sub-population of K2P channels. TREK1 channels are polymodal transducers of different cellular stimuli [39], [40], like mechanical pressure or pH shifts that transduce into changes of V_m , so that any distinction between steady-state and activated state of these and most of others K2P channels requires careful consideration, both experimental and biophysical. Working with steady-state recordings from astrocytes isolated in a bath assures that obtained I-V curves represent cells in steady conditions, non-transducing an osmolar stress or pH variations, which is implicitly assumed in a baseline model.

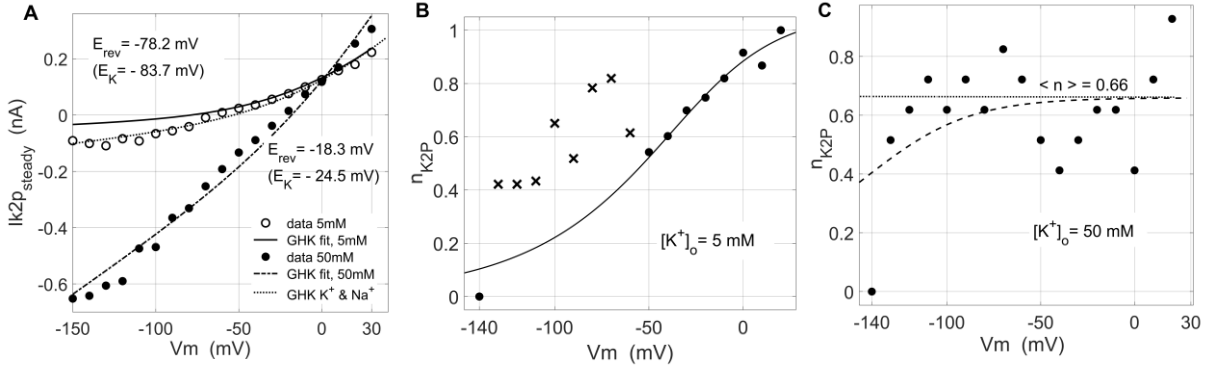


Figure 5 - Steady-state I-V relationships and activation kinetics of K2P-TREK1 currents in astrocytes – (A) Steady-state I-V characteristics of K2P-TREK1 currents fitted with the Goldman-Hodgkin-Katz current equation, for $[K^+]_o = 5\text{mM}$ (circles/solid line) and 50mM (filled circles/dashed line). The dotted curve shows the fit corrected with a small Na^+ permeability being added ($P_{Na^+}/P_{K^+} = 0.06$, see text). **(B)** and **(C)** Approximation of the activation kinetics $n_{K2P}(V)$ of K2P current for $[K^+]_o = 5\text{mM}$ and 50mM respectively, obtained as $(g_{slope} / \bar{g}_{max})^{1/k}$, $k = 2$, see text. At 5mM , in (B), the n_{K2P} activation estimates for V_m positive to -50mV (filled circles) were fitted with Boltzmann first-order activation kinetics, ignoring more negative V_m values where very small currents produced erratic estimates of g_{slope} , obtained by numerical differentiation (crosses). **(C)** The loss of voltage-dependent activation n_{K2P} (as seen in B) at $[K^+]_o = 50\text{mM}$ was modeled as a gradual $[K^+]_o$ -dependent shift of the n_{K2P} curve (see Eq. 12b) to the left practically removing the sigmoidal voltage dependence and reducing n_{K2P} to fluctuations around a mean, constant activation $\langle n_{K2P} \rangle = 0.66$, for voltages in the activated range for K2P current.

Apart from the outward voltage activation (verified also in a symmetrical K^+ concentrations), K2P channels show also some form of *flux-dependent activation* component coming from multi-ion occupancy of the pore by the permeant K^+ ions [28]. The following two dynamical properties in voltage-dependent activation of K2P-TREK1 current are essential for arriving at the full dynamic model of V_m :

- **Activation kinetics** - At both concentrations, the whole-cell currents showed activation kinetics with $\tau_{K2P} \approx 3\text{ms}$, constant over the whole V_m range. While at 5mM , above -50mV we could fit a Boltzmann sigmoidal, voltage-dependent activation, Fig. 5B black dots, at drastically elevated, $[K^+]_o = 50\text{mM}$ there is no visible voltage dependence, Fig. 5C, described with a constant average activation of $\langle n_{K2P} \rangle = 0.66$.
- **Gating mode change** – At elevated external K^+ , Fig. 5A, the dominating *electrochemical activation* [28] is changing the I-V curve, resembling more that of the leaky K2P-TWIK channels with almost linear dependence, satisfying the GHK current equation and reversing close to the Nernst potential.

Along with these observations we model the astrocytic K2P-TREK1 currents using the GHK current model [37], extended with a complex electrochemical activation n_{K2P} – coupling the voltage-dependent activation and electrochemical driving force into a mechanism named *ion-flux gating* [28]:

$$\begin{aligned}
 I_{K2P} &= n_{K2P}^k I_{K2P-GHK} \\
 &= n_{K2P}^k P_{K2P} \frac{F^2 z_{K2P}^2}{RT} V_m \frac{([K^+]_i - [K^+]_o \exp(-z_{K2P} V_m / v_s))}{(1 - \exp(-z_{K2P} V_m / v_s))} \quad (nA).
 \end{aligned} \tag{11}$$

Allowing for variations of K^+ concentrations we cannot keep the intrinsic permeability P_{K2P} constant [41], contrary to the classical assumptions based on the solubility-diffusion theory [26], [42]. To add a simple $[K^+]_o$ dependence in P_{K2P} we interpolated the fitted values for P_{K2P} at 5mM and 50mM with an increasing and slowly saturating K^+ dependence, Eq. 12a. The GHK fit at 5mM suggested $P_{K2P}^b = 1.24 \times 10^{-8}\text{cm/s}$ for the baseline permeability, within the order of magnitude with those reported in the early studies of electro-diffusion in K^+ channels, [43]. As an additional sanity check, the ratio $P_K/P_{K2P} = 6.15$ of the constant permeability values obtained by fitting the GHK models of the Kir I_{res} and I_{K2P} , is reasonably close to 5.3, the ratio of their maximal measured values at 30mV , Fig. 1.

Fitting of the sigmoid in Fig.5B to $(g_{slope} / \bar{g}_{max})^{(1/k)}$ graph obtained by differentiation for both concentrations was done with $k = 2$, following as a guiding value the average ion occupancy of the SF with $2.2 e_0$ elementary charge units across different K2P channel subtypes, estimated in [28]. Small voltage offset $(V_m - V_{ofs})$ not exceeding $5 mV$ was needed to stabilize numerically the nonlinear LSQ fitting of (11). The same value $z_{K2P} = 1$ was used at both K^+ concentrations.

The nominal, baseline external concentration $[K^+]_o^b$ was kept at $2.5 mM$ in Eq. 12a. To correct the n_{K2P} activation for variable concentrations two interventions are needed: (i) decreasing trend of the maximal activation with $[K^+]_o$, Eq. 12b, where the $[K^+]_o/[K^+]_i$ term successfully captures the trend, and (ii) shifting the V_{12-K2P} (12c) and the whole n_{K2P} sigmoid to the left (into non-physiological hyperpolarized range) so that the plateau of $\langle n_{K2P} \rangle = 0.66$ covers the most of physiological V_m range - practically removing voltage-dependent activation at high $[K^+]_o$, Fig. 5C. More recordings on different $[K^+]_o$ are needed to verify whether the suggested corrections in Eq. 12b and Eq. 12c have more general biophysical utility. The relative shift of Nernstian nature in (12c) required a scaling factor $S = 1.7$ to get the plateau-like in Fig. 5C. Similar proportionality of V_{12} shift was observed in activation curves of the human K2P-TREK1 channels expressed in *Xenopus* oocytes [28].

$$P_{K2P} = P_{K2P}^b (1 + 0.85 \log_{10}([K^+]_o/[K^+]_o^b)) \quad (cm/s), \quad (12a)$$

$$n_{K2P}(V, [K^+]_o) = \frac{1 - [K^+]_o/[K^+]_i}{(1 + \exp(-z_{K2P}F(V - V_{12-K2P})/RT))}, \quad (12b)$$

$$V_{12-K2P}([K^+]_o) = V_{12-K2P}^0 - S v_s \ln([K^+]_o/[K^+]_o^b) \quad (mV). \quad (12c)$$

Equation 11 fuses (i) the modified voltage-dependent and $[K^+]_o$ -corrected n_{K2P} activation, Eq. 12b, describing an arbitrary K2P channel population, and (ii) the nonlinear Goldman-Hodgkin-Katz electro-diffusion describing the macroscopic steady-state current of the whole, voltage-clamped cell. The GHK current model extended with activation kinetics has already been used in descriptions of neuronal voltage-gated calcium channels [44].

2.3 Full model of glial V_m dynamics – The dynamics of the astrocytic membrane voltage V_m is described by the differential equations Eq. 13, where to Kirchhoff's current law a single kinetics equation has been coupled, that of K2P channel activation n .

$$\begin{aligned} C_m dV_m/dt &= -(I_{Kir} + I_{K2P} + I_{leak}) + I_{ext} \quad (nA) \\ dn/dt &= (n_{K2P}(V_m) - n)/\tau_{K2P}. \end{aligned} \quad (13)$$

An unspecific, potassium Ohmic leak current is added as $I_{leak} = g_{leak}(V_m - E_K)$ with the conductance not exceeding 15% of the chord conductance of total glial K^+ current in the I-V plot, proportional to the current that remains after isolating Kir and K2P currents, Fig 1.

The external inputs, resembling external currents to an astrocyte *in situ*, are represented as:

$$\begin{aligned} I_{ext} &= I_{gjc} + I_{lfp} \quad (nA) \\ I_{gjc} &\sim \sum_i g_c^i (V_m^i - V_m) = const. \quad (nA) \quad i = 1, \dots, N_{neighbors} \\ I_{lfp}(t) &= g_{lfp} V_{lfp}(t) \quad (nA), \end{aligned} \quad (14)$$

where I_{gjc} brings in the contribution from all neighboring astrocytes connected via Ohmic gap junction connections (GJCs) and will be varied as a parameter, while $I_{lfp}(t)$ represent the transient, variable depolarizations of the membrane coming from the changing local field potential immediate to the astrocytic membrane, resulting from prolonged neuronal spiking episodes.

Parameter	Units	Description	Value, default	Comment
T	K	Temperature	298	Room temperature, 25°C in [12]
F	C/mol	Faraday constant	96485	
R	$J/mol \cdot K$	Universal gas constant	8.314	
v_k	mV	Slope factor, RT/F	25.7	at $T = 298^{\circ}K$, constant in all models and simulations
$[K^+]_o^{nom}$	mM	Baseline $[K^+]_o$ in extracellular space	2.5 – 5	5mM used in I-V fitting, varied within param. analysis
$[K^+]_i$	mM	Astrocytic $[K^+]_i$	130	
C_m	pF	Astrocytic membrane capacitance	20	Mean effective capacitance of the patch, whole-cell
\bar{g}_{s-inw}	μS	Max. Kir inward slope conductance	0.00917	Hagiwara model of Kir current, Eq. 3
A	$1/mM^{1/2}$	Dim. constant, correcting for $\sqrt{[K^+]_o}$	1	Dimensionality correction
V_{12-nom}	mV	Half-activation voltage V_{12} at $[K^+]_o^{nom}$	-53.5	Hagiwara model of Kir current, Eq. 3
z_{inw}		Effective charge valence, I_{Kir}	1.638	Hagiwara model of Kir current, Eq. 3
z		Unitary valence of permeant K^+ ions	1.0	
$E_{rev-Kir}$	mV	Rev. voltage of isolated Kir4.1 current	-76	Average exp. measured reverse voltage
P_K	cm/s	Constant permeability of K^+ in pores	7.63e-08	K^+ permeability in classical Nernst-Planck formalism
$V_{12-out0}$	mV	Half-activation voltage of I_{res}	-51.4	Boltzmann term in p_0 , Eq. 6
z_B		Effective charge valence of the blocker	1.6	Mg^{2+} or polyamine blocking ion
G_0	RT units	Voltage-independent entry barrier	6.6	Barrier height at x_T , Marcus term, Eq. 7
l_{SP}		Normalized, unitary length of the pore	1	Short pore model, Fig. A1
x_T		Fractional distance of transition state	1/2	Position relative to the beginning of the pore
λ		Half-width of the energy wells	1/4	Marcus term, Eq. 7 and Fig. 3
δ		Fractional, electrical length of the pore	1/2	Fraction of l_{SP} over which V_m drops, Marcus term, Eq. 7
V_{12-K2P}^0	mV	Half activation voltage V_{12} at $[K^+]_o^{nom}$	-20.5	I_{K2P} model, n_{K2P} activation, Eq. 12c
k		k-th power in K2P activation kinetics	2	Hodgkin-Huxley formalism, Eq. 11
S		Scaling parameter in n_{K2P} activation	1.7	Adjusts the shift of n_{K2P} with $[K^+]_o$, Eq. 12c
z_{K2P}		Charge valence for K2P pores, fixed	1.0	I_{K2P} model, Eq. 11 and n_{K2P} activation, Eq. 12b
τ_{K2P}	ms	Activation time of K2P-TREK pore	3.0	From exp. data [12], Eq. 12b
P_{K2P}^b	cm/s	K2P channel permeability, basal	1.24e-08	I_{K2P} model, GHK description, Eq. 12a,
g_{leak}	μS	Glial leak conductance, Ohmic	0.001-0.002	Non-specific leak, glial voltage dynamics, Eq. 13
I_{ext}	nA	External current to the astrocyte	0.2 - 0.4	Glial voltage dynamics, Eq. 13
g_{lfp}	μS	Transfer conductance in resp. to V_{lfp}	0.01-0.016	Adjusted to the I_{ext} ranges in bifurcation analysis

Table 1 – Parameter values used in the fitting of current models, parametric analysis, and simulations of the full system, Eq. 13.

It has been already shown that Eq. 13 represents a minimal model where only K^+ conductances, without any Na^+ or Ca^{2+} contributions could produce more complex dynamical behavior of V_m than a stable fixed point V_r [19].

Table 1. contains all the parameter values and/or value ranges used in the dynamical analysis of the model and the numerical simulations of transiently perturbed behavior.

3. Results

3.1 Parametric analysis of the V_m dynamics

To translate the nature and intensity of the perturbations in different experimental preparations into changes of model parameters, we refer to (a) *static*³ alterations of the astrocytic K^+ conductances for changes manifesting in the steady-state I-V relationships, and to (b) *dynamical perturbations* of V_m in Eq. 13 for response to transient changes in the local field potential, depolarizations through the gap-junctions, or response to transient shifts of $[K^+]_o$.

Of not many disease modeling studies differentially isolating glial currents (mostly focusing on Kir), we looked for those where the changes *would* alter the monotonic I-V dependence of the total astrocytic current, Fig. 1. For the nature of current alterations, and the source references see Table A2 in Appendix 2. Sole focus on Kir currents with K2P current not being isolated has prevented those studies to report the impact of altered Kir current on the I-V curve of total current. The alterations of Kir currents summarized in Table A2 suggest that the model should consider asymmetrical changes of Kir conductivity in different V_m ranges, either as a hallmark of a pathology or different functional channel expressions like in the case of heteromeric Kir4.1/Kir5.1 channels. Biophysical specificity of the Kir4.1/Kir5.1 channel is that it turns weakly rectifying Kir4.1 into a strong inward rectifier [45], numerically equivalent to almost fully attenuating the outward I_{res} current.

Figure 6A illustrates the trend of change in the steady-state I-V curve of the total K^+ current in different scenarios of Kir deregulation in Table A2. A typical effect is a loss of monotonicity positive to $+60$ mV, where both Kir4.1 and K2P currents coexist producing a non-monotonous N-shaped I-V curve. In Figure 6A we sketched this effect by different attenuations of Kir inward and/or outward component using our model, based on the I-V graphs in different disease models, Table A2. Included also, the lower solid curve, is the combined effect of loss of outward Kir conductance in parallel with drastically increased $[K^+]_o$ like in cases of seizures and spreading depolarizations. To produce the effects in Fig. 6A we were (a) decreasing \bar{g}_{S-inw} for the inward range of WR-Kir current in the Hagiwara model, Eq. 3, and (b) doing the same using a multiplier in the GHK model, Eq. 8 for the outward range, due to a complex form of the conductance in I_{res} model. The K2P current was kept in the nominal range and shape.

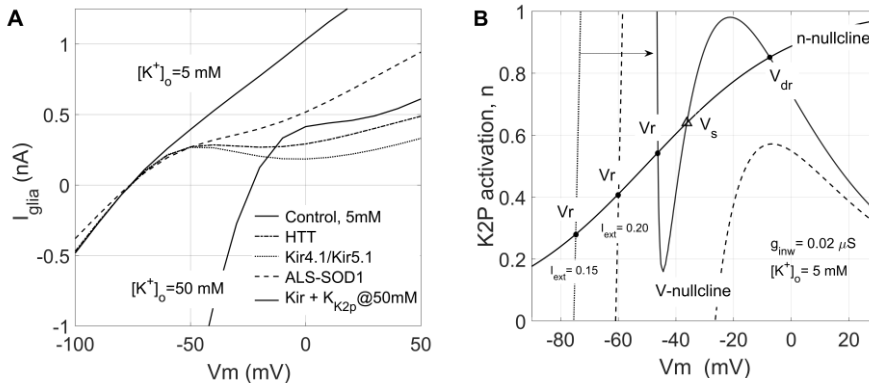


Figure 6 – Loss of monotonic I-V curve via alterations of Kir4.1 currents in disease models. (A) Alterations in Kir conductivity without changes in K2P conductance produce non-monotonic I-V curves. The lower solid curve illustrates the parallel effect of a drastic increase in external K^+ , while all others are obtained by amplifying or attenuating the Kir currents in Eq. 13, at $[K^+]_o = 5$ mM based on the nature of deregulation in Table A2, Appendix 2. The labels in the legend relate each curve to the corresponding study in Table A2. (B) Example of nullcline analysis in (V_m, n) plane. Increasing the constant I_{ext} changes (into an N-shape) and shifts the V-nullcline introducing a saddle fixed point V_s (triangle), and markedly more positive stable node or focus V_{dr} via the fold bifurcation. The dotted, dashed, and the solid line show the changing shape of the V-nullcline with I_{ext} .

Since the typical dynamic perturbations, same as with neurons, transiently depolarize the glial membrane by I_{gjc} or $I_{lfp}(t)$ currents, the principal bifurcation parameter was a constant in time I_{ext} .

³ Even though the experiments observe real-time channel expressions changes, those happen on time scales of minutes, hours or longer, which warrants keeping the corresponding parameters constant on timescales of milliseconds or seconds.

As a second bifurcation parameter, we varied \bar{g}_{s-inw} and $[K^+]_o$ with attenuation of I_{res} as a static perturbation of the model, so that all scenarios of impact on Kir conductivity could be implemented.

In the 2-dimensional system, Eq. 13, using nullclines let us detect the trends of change in the phase portrait. As expected and previously illustrated in models of neurons very similar to Eq. 13 [19], chapter 5, in addition to the nominal equilibrium state V_r - a stable node for V_m slightly more positive to E_K , the N-shaped I-V curve introduces a second stable node via the fold bifurcation, as we vary I_{ext} , Fig. 6B. The fold bifurcation is generic in 2-d models like Eq. 13 with N-shaped nonlinearity in the voltage⁴ equation and robustly observed within wide parameter ranges. We keep referring in the rest of the text to the nominal stable, resting state as V_r , and to the more depolarized, again stable steady-state introduced by the fold bifurcation as V_{dr} .

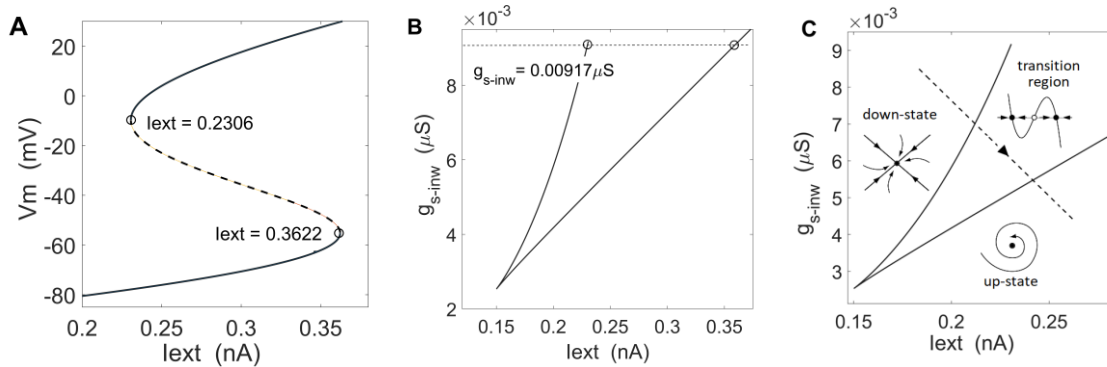


Figure 7 – Fold bifurcations in (V_m, n_{K2P}) dynamics are generic when the perturbed model displays an N-shaped I-V characteristic. (A) Fold bifurcation diagram of Eq. 13 for $g_{s-inw} = 0.00917 \mu S$, with $I_{res} = 0$. (B) A cusp curve in (I_{ext}, g_{s-inw}) plane obtained by running 2-parameter continuation from the fold point at $I_{ext} = 0.2306$ in (A). The coordinates of the corresponding stable steady states are $(V_r = -77.86 \text{ mV}, n_{K2P} = 0.0964)$, and of the saddle-node close to $(V_{dr} = -9.734 \text{ mV}, n_{K2P} = 0.6)$, with g_{s-inw} kept at the same value as in (A). (C) The dashed line shows a typical path through the parameter plane corresponding to a membrane with deregulated Kir conductance perturbed by a net depolarizing current I_{ext} . The region bounded by the cusp curve separates the two *monostable* parameter domains, the down-state domain, corresponding to the true nominal resting state V_r (of node type), and that of the up-state, corresponding to a *single* depolarized steady state V_{dr} , of focus/spiral type. For parameter values inside the transition region, within the cusp, the model displays two stable nodes separated by an unstable saddle point.

Figure 7A and 7B show the fold and cusp bifurcation diagrams for changing I_{ext} and g_{s-inw} , with the outward I_{res} attenuated. All continuations were done using the *AUTO* package [46] as implemented within *XPPAUT* [47]. Examples in Fig.7A and 7B were computed with $I_{res} = 0$, though qualitatively the same behavior is present with I_{res} between zero and 15% of its intensity. All other model parameters were kept at the values given in Table 1, used in the fitting of steady-state I-V characteristics, with $[K^+]_o = 2.5 \text{ mM}$ and the glial leak $g_{leak} = 0.0013 \mu S$. At $I_{ext} = 0.2306 \text{ nA}$, in Fig. 7A the bifurcation introduces a saddle-node at $V_{dr} = -9.734 \text{ mV}$, notably depolarized to the nominal $V_r = -77.86 \text{ mV}$, which further splits into a saddle and stable node at V_{dr} as I_{ext} further increases. The cusp curve Fig. 7B fusing fold bifurcation behavior of two parameters divides the (I_{ext}, g_{s-inw}) plane in three regions: (I) the *down-state* represented by V_r , (II) the *up-state* represented by the depolarized resting voltage V_{dr} of type focus, and (III) the bistability region where V_m transits towards either of the stable nodes, qualifying the model for switching behavior. Equations 13 represent the first minimal ODE model of the glial membrane near V_r , based on whole-cell recordings, suggesting the existence of a stable, depolarized up-state in glial V_m dynamics, within a wide range of parameters.

The biological relevance of downregulating or abolishing the WR-Kir outward I_{res} current as a parametric perturbation is directly suggested by (i) electrophysiological data in several disease models we listed [48], [49], as well as (ii) by the specific properties of heteromeric Kir4.1/Kir5.1 channel populations [50], [45]. The later accounts for a nonnegligible fraction of Kir4.1/Kir5.1 channels in astrocytes in different brain regions [51], [52], [12]. The extent of deregulation of the

⁴ We refer to the first ODE in Eq. 13 as *voltage equation* because it describes the dV_m/dt derivative, even though as a physical law it is the Kirchhoff's current equation.

inward conductance of the Kir4.1 alone – a decreased slope in the I-V curve negative to V_r , is not detrimental for the observed qualitative changes since it doesn't produce by itself the N-shaped I-V curve.

The dashed line in Fig. 7C represents a typical *perturbation line* of Eq. 13 combining (i) permanent deregulation of outward conductance of WR-Kir, with (ii) changing inward WR-Kir conductance in experimental conditions where an astrocyte is (iii) subjected to depolarizing current input I_{ext} .

Slow depolarizations induced by K^+ accumulation in extracellular space (ECS), and subsequently the positive shift of E_K and V_r suggest that either as a parameter, a transient perturbation, or a slow variable in an extended 3-dimensional model, $[K^+]_o$ could be inducing instability of V_r . Since an extension of the system, Eq. 13 incorporating $[K^+]_o$ dynamics in R^3 or higher [53] is beyond the scope of this study, we verified that fold and cusp are robust in $(I_{ext}, [K^+]_o)$ parameter domains as well, with I_{ext} in the same range as above, and $[K^+]_o$ modestly raised compared to the nominal 2.5 mM, Fig. 8. It is important to report that higher the $[K^+]_o$ much less pronounced attenuation of I_{res} produces the N-shaped curve and the fold bifurcation, (much less than 85%).

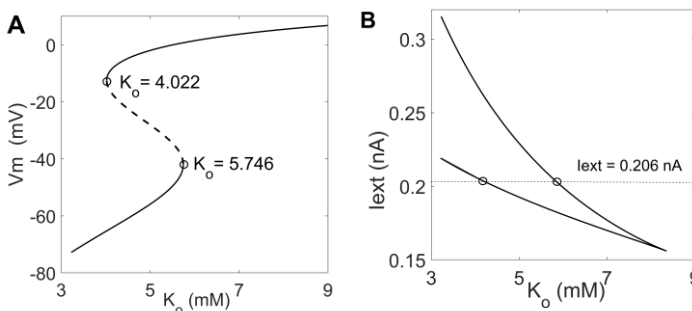


Figure 8 - Fold bifurcations under variable $[K^+]_o$ with abolished I_{res} (A) Fold bifurcation in Eq. 13 for variable $[K^+]_o$, keeping $g_{s-inw} = 0.00951 \mu S$. (B) A cusp curve in $(I_{ext}, [K^+]_o)$ plane obtained by running 2-parameter continuation from the fold point at $[K^+]_o = 4.022$ in (A). The actual continuations in XPPAUT were computed using E_K due to better numerical convergence. $[K^+]_o = 4.022$ mM corresponds to $E_K = -89.32$ mV, for $[K^+]_i = 130$ mM.

Large separation of time scales between V_m responses and $[K^+]_o$ transients, from milliseconds to second and minutes, warrants analyzing the basic $[K^+]_o$ impacts on V_r stability treating it as a parameter in the simple 2-dimensional system, Eq. 13.

Quantitative studies summarizing the properties of macroscopic currents through the glial Kir4.1 [54] and K2P-TREK channels [28], [37] suggest that apart from K2P activation there is no other channel kinetics critical to extend the minimal model, Eq. 13, with additional dynamical variable. Whole-cell Kir4.1 responses to voltage clamp commands suggested almost instantaneous activation with rising times of less than 2 ms. The instantaneous Kir4.1 currents, measured at 2 ms, were somewhat higher in the mid and outward range but not producing qualitative change in I-V curve. There is therefore no candidate for a *resonant variable* in the 2-D model, Eq. 13, [19], [55] which would induce a cyclic behavior in \mathbb{R}^2 . A word of caution is needed in this context due to the measurement difficulties with the leaky astrocytic membrane patches. Inability to precisely determine the input and access resistance of the patched astrocyte [1] makes it unreliable to compensate for the serial loss, which in turn always produces underestimated maxima of both, instantaneous and steady currents potentially compromising our judgment on the rise times in the current responses to voltage commands.

3.2 Numerical simulations of the bistability and switching

For demonstrating the switching capability we perturbed the model, Eq. 13, using time series from recordings of glial depolarization during *electrographic seizures* induced by transient elevation of $[K^+]_o$ [9]. The glial V_m was recorded using two-electrode *in-situ* protocol on glial membrane in rodent hippocampal slices.

Figure 9, (upper trace) shows a sample of glial depolarization ΔV_{ext} in response to neuronal seizure, Fig. 11A in [9], digitized from a printed image using the *Graph Grabber* tool [56]. Such signal features: (i) a fast depolarizing, tonic transient of $\Delta V_m \approx 20$ mV within initial ten seconds, followed by (ii) pseudo-periodic clonic episodes lasting in total for nearly 60 seconds. To use the ΔV_{lfp} recording as a perturbing signal in our model we needed somewhat realistic time course of the corresponding

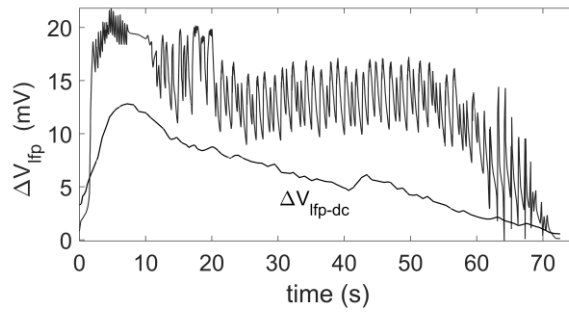
$\Delta E_K(t)$ shift, for which purpose we used ΔV_{ext-dc} averaged signal of 27 seizure events (from 5 cells) from the same study [9] see Fig. 10A, plotted as a lower curve in Figure 9 below, so that for a realistic example of I_{ext} in Eq. 14 we get:

$$\begin{aligned}
 I_{ext}(t) &= I_{gjc} + I_{lfp}(t) = I_{gjc} + g_{lfp}\Delta V_{ext}(t) \quad (nA) \\
 E_K(t) &= E_K + \Delta E_K(t) \approx E_K + \Delta V_{ext-dc}(t) \quad (mV) \\
 \Delta V_{ext}(t) &= V_{glia}(t) - V_{lfp}(t); \quad \Delta V_{ext-dc} = \langle \Delta V_{ext} \rangle - \langle \Delta V_{lfp} \rangle \quad (mV).
 \end{aligned} \tag{15}$$

The $V_{ext}(t)$ signals were measured with a reference to a distant ground in the bath and should be referenced to the LFP level immediately adjacent to the cell measured the same way [9]. That correction averaged at 3 mV, was omitted in the final simulations since it produced no difference and would in principle cancel out in $(V_{ext} - E_K)$ if such control measurement of externally generated driving force existed.

Perturbation signals as in Eq. 15 mimic a transient depolarization event of a hippocampal glial cell *in situ* - depolarized by a positive, outward current resulting from sustained seizure-like discharges invading the surrounding neurons in a larger region, slowly and transiently elevating, and restoring the nominal $[K^+]_o$ during 72.6 seconds. We do not use it to simulate bath application of a constant elevated $[K^+]_o$ in [9], but try to simulate more realistic transient depolarization which in reality comes with transiently altered local $\Delta E_K(t)$.

Figure 9 – Transient glial depolarization signals – Depolarization transient ΔV_{lfp} from resting (upper trace) measured on glial soma *in situ*, in response to an electrographic seizure initiated by increased $[K^+]_o$ to 8.5 mM, in a rat hippocampal slice. A two-electrode protocol was used with a reference electrode in the bath. ΔV_{lfp-dc} (lower trace) is an average of 135 depolarizing episodes, recorded from 5 cells, used to approximate the shift of the Nernstian potential $\Delta E_K(t)$ due to K^+ accumulation.



We find ΔV_{ext-dc} to be a good example of $\Delta E_K(t)$ transient assuming it represents an average of LFP events that (a) in reality are subjected to low-pass filtering of the ECS [57] which will reduce them to the slower timescales typical for gradual $[K^+]_o$ changes, and (b) are of common shape in the initial steady depolarization phase, time-aligned at the onset. Its maximal amplitude of 12.8 mV is close to the Nernstian $\Delta E_K = 13.7$ mV, for a relative shift from $[K^+]_o$ at the nominal 5 mM in our data (the nominal I-V relations in the model), to 8.5 mM bath concentration robustly producing the seizures [9]. The slower rise time in the initial 10 seconds, as well as the steady decay of the averaged $\Delta V_{ext-dc}(t)$ probably reflect the joint action of the Na-K pump and other restorative mechanisms of ion homeostasis. Such $\Delta E_K(t)$ is therefore a safe approximation for low to moderate $[K^+]_o$ increases on the timescale of seconds, even a more conservative one, producing slightly less depolarized E_K shifts if we start from a baseline of 2.5 mM of external K^+ . Unspecific conductance g_{lfp} was introduced to convert the transient voltage perturbation $\Delta V_{ext}(t)$ into current perturbation signal in Eq. 15. Indicative value range of g_{lfp} was set between $0.01 \div 0.016 \mu S$ to keep the total $I_{ext}(t)$ in simulations within the range of the fold bifurcation diagram, Fig. 7A, matching the dynamic range of the clonic discharges in ΔV_{ext} of $5 \div 10$ mV, from $t = 10$ s onwards, Fig. 9.

A simulated example of switching behavior in response to the above perturbing transients is illustrated in Figure 10. We observed two qualitative behaviors depending on I_{res} attenuation and I_{ext} and g_{s-inw} value ranges. With fully abolished outward I_{res} , constant $I_{gjc} = 0.125$ nA and nominal $g_{s-inw} = 0.00917 \mu S$ at $[K^+]_o = 2.5$ mM, Fig. 10A shows a series of *plateau responses* on ΔV_{ext} from Fig. 9, with $0.01 \leq g_{lfp} \leq 0.017$. With increasing g_{lfp} the response switched from the downstate to the upstate in a threshold manner – from partially to fully. With I_{res} attenuated to 15%

of its amplitude, a more *erratic switching* profile without prolonged upstate was a typical response, shown in Fig. 10B with the other parameters kept the same.

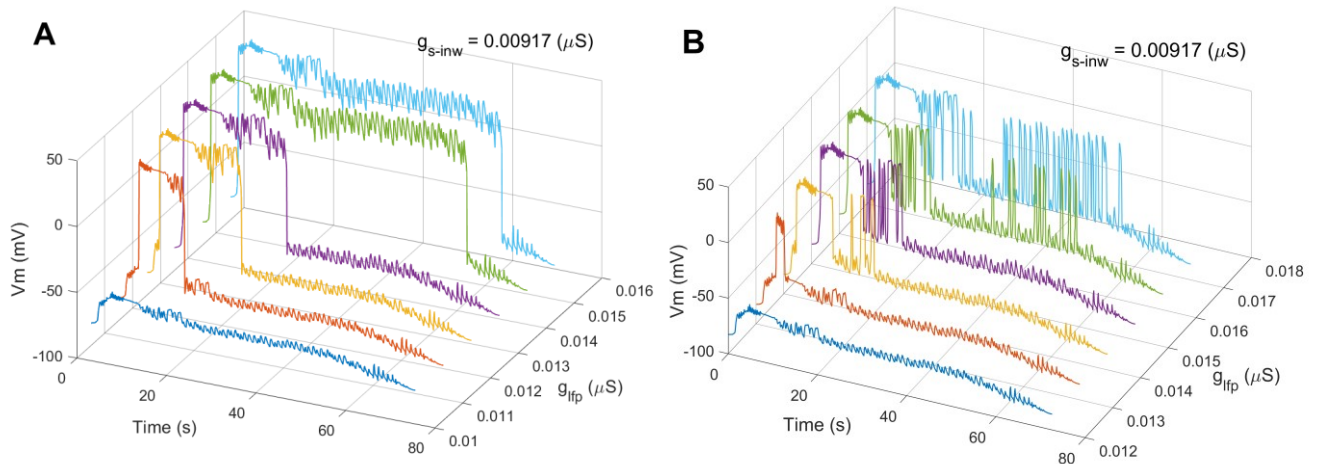


Figure 10 – Glial switching on transient seizure-like perturbation – (A) Simulations of the full model V_m response on electrographic seizure, Fig. 9, with fully abolished Kir outward I_{res} current and increasing g_{lfp} show plateau switching between downstate and upstate, corresponding to V_r and V_{dr} . **(B)** The same simulation, with I_{res} amplitude reduced to 15%, demonstrating an irregular, erratic switching with a frequency following that of the clonic phase of seizure signal. The presence of I_{res} shifts both V_r and V_{dr} slightly more negative. A constant level of external current through gap junctions was kept at $I_{gjc} = 0.125$ nA and the slope of Kir inward conductance was held at the nominal $g_{s-inw} = 0.00917$ μ S.

Decreasing Kir inward current, via g_{s-inw} led to more pronounced instability and more frequent switching in either profile for lower transfer conductance g_{lfp} , see Figure S1 in *Supplementary Information*. No particular, numerical sensitivity in any of the parameters was observed indicating a more peculiar singular behavior, in dynamical terms.

4. Discussion / I ~ importance, S – significance, N – novelty, U - utility /

The observed dynamical instability could point to different areas of impact depending on the physical model system and the specific V_m dependence of the modeled phenomenon. A general conclusion in hypothesis-free terms would be that with its very basic ion channel composition the glial membrane responds differently and distinctly to external depolarizations when Kir or combinations of Kir and K2P conductances are deregulated, due to the interplay of Ohmic and complex non-Ohmic conductances, nonlinear in V_m . Below, we discuss the possible implications of the presented biophysics from several different neurobiological perspectives.

4.1 On the model

(11) Numerous biological *association studies* have related, *put in context* the changes in expression of Kir4.1 currents and the biophysical properties of measured currents to the altered function of glia. In translating such changes into specific roles of the cell, it has remained elusive which mechanisms could transduce the molecular changes into a whole-cell voltage response. We modeled V_m dynamic of an isolated astrocyte by a minimal ODE model incorporating the major K^+ conductances, WR-Kir and K2P, and a leak current to explore the direct effect of nonlinear changes in the total astrocytic ion conductance to V_m dynamics. In other words, it models the simplest form of modulation of V_m by alterations of ion conductances with no other signal transductions being modeled, like membrane mechano-sensitivity, pH sensitivity, actions of physiological agonists, etc. The model, Eq. 13, let us ask the typical question - which nature of (de)regulation of the conductances impacts the stability of the nominal resting state V_r , which in turn controls all electrogenic transport mechanisms.

(12) Decades of conductance-based models suggest that even very small currents need careful consideration since the nonlinear interplay of their conductances could impact the stability of the resting state and in turn the cell response [19]. That has motivated the incorporation of the K2P current through its activation dynamics, $n(t)$, as a second dynamical variable.

The major perturbations of the baseline model came from decreased Kir conductance in the outward V_m range, with K2P conductance remaining unchanged or eventually increased, resulting in a non-monotonic steady-state I-V curve. **(N1)** In that regard we present the first ODE model of glial V_m , Eq. 13 which incorporates two distinct and *differentially regulated* K^+ currents, in addition to the unspecific K^+ leak current, based on recordings from isolated cells.

(S1) Non-monotonous, N-shaped I-V relation produced by a prominent decrease of WR-Kir in the outward range, gives birth to a new, more depolarized *stable* steady state V_{dr} for physiological average external depolarizing current, I_{ext} . When present, such a mathematical feature of a model of a non-excitable cell is generic and observed robustly in a wider parameter range, Fig. 7. We argue here that the emergence of a distinct and stable V_{dr} introduces a specific and distinctive transition - translating the loss of pseudo-Ohmic, linear behavior of the membrane into a *bistable switch* when exposed to depolarizing transients, Fig. 9. Bistable switches with or without hysteresis are pervasive and diverse in biological systems since those are the simplest outcomes of instabilities of the resting state [58]. An elegant analytical model of the same form of bistability in hypokalemic skeletal muscle is presented in [59].

To simulate the switching between V_r and V_{dr} using a perturbation specific to the repertoire of real glial cells we used a seizure-like transient recorded on glia rather than a ramp or constant I_{ext} , since glial cells in real circuits do not receive prolonged depolarizations by constant external currents. We believe the chosen electrographic seizure has a typical waveform for a wider range of strong transient depolarizations resulting from coherent discharges of hippocampal neurons.

In modeling open, background Kir channels we departed from the typical modeling approach, a single current – single biophysical description. The reversal of polarity of the driving force changes the nature of the physiological block resulting in *qualitatively different pseudo-gating in the WR-Kir pore for inward and outward flux* (Appendix A). This assumption warrants the use two different biophysical descriptions for additive inward and outward fluxes. Figure 3 suggests that this conceptual approach results in an overlapping V_m regions where both mechanisms (blue and red curve in Fig.3) produce a small outward current. Those outward permeation events happen for very small ΔV_m where the electrical enthalpic contributions are comparable to the fluctuations – resulting in outward pseudo-gating in the central cavity, as well as within the SF, described respectively by the Hagiwara model, and by the nonconstant-field GHK equation, Eq. 5. Such different gating scenarios require several effective charge valences z_{inw} , z_B , and z to appear within descriptions of WR-Kir current. The equivalence of the form of nonconstant-field GHK model of I_{res} , Eq. 8, and the basic form of rate model based on simplified Eyring's formalism with a single, centered, and symmetrical barrier [42], together with the attempts to relate Hagiwara's model to multi-barrier Eyring model [60] suggest at least an opportunity to consider bringing the proposed separate models of WR-Kir inward and outward fluxes under a more coherent formalism.

(N2) Departing from the constant field assumption in the Nernst-Planck formalism of an open pore, results in a modified Goldman-Hodgkin-Katz current equation which allows incorporating simple forms of nonlinear energy profiles within the pore, as long as the integral in the current equation is solvable [27]. We applied it for the first time to describe the outward component of WR-Kir current, Eq. 8, and by extending it with quadratic dependence of the barrier peak, Eq. 7, the observed current saturation with voltage was captured by the model, Fig. 4. Accumulating evidence of complex gating in open pores, lacking a voltage-sensitive gate, may qualify this approach in a wide range of leaky channels.

Preliminary extension of Eq. 13 we attempted with $[K^+]_o$ dynamics [53], [61], [62] *in a very simplified, spatially constrained ECS* compartment demonstrated an enriched dynamical repertoire of the model and will be reported in another study. Within $[K^+]_o$ ranges indicating the richer bifurcation repertoire in [53] and [63], we observed some entrainment of the glial V_m in Eq. 13 by the $[K^+]_o$ dynamics driven by a coupled neuronal bursting [53], but those require more precise dynamical characterization. Other important extensions of the model should include (a) incorporating the chloride conductances explicitly and (b) adding mechanosensitivity to K2P conductances to simulate the osmolar stress of the membrane.

Very limited availability of transient recordings from glia leaves us without traces of real-time perturbations of glial V_m on different time scales which is a limiting factor to considering a *non-autonomous, driven ODE* in the model Eq. 13, since in immediate proximity of spiking neurons the glial cells are never in a true voltage steady state. An isolated astrocyte is not a biological reality but has been an experimental and modeling target system for detecting and describing the baseline cell properties. The heavily interconnected glial cells in the *glial cell continuum* require testing any indications of V_m multistability using spatially extended models in the light of experimentally observed V_m *isopotentiality* [64] – a tendency of interconnected glia to quench any marked depolarization.

4.2 On the instability and glia

(S2), (N3) Translating V_m bistability and altered WR-Kir current into effects significant for the whole cell function, the following impacts are directly implicated by the model:

- **Depolarized resting state V_{dr} as a catastrophic event⁵** – Even though it is one of the simplest instability scenarios, the birth of a stable, very depolarized resting state is potentially *catastrophic* since switching to $V_{dr} > -10 \text{ mV}$ is taking the membrane and the cell, to a state with much higher potential energy than the nominal hyperpolarized resting state, not corresponding to the actual $[K^+]_o$. Prolonged depolarization of the glial membrane around V_{dr} would impact all glial functions, from metabolic support to membrane transport, and practically all neuromodulatory roles assigned to glia.
- **(I3) Voltage switching between V_r and V_{dr} disrupts the kinetics of active transport mechanisms** - Since all major electrogenic pumps and transporters show some extent of voltage dependence [68], [69], [70], the depolarized V_{dr} , or the up-state should violate the assumptions made for the steady-state transport rates near V_r . In the case of ATP-driven pumps, in the Na-K pump, for example, all simplified descriptions used in computational models, in a form of a simple current generator $I_{pump} = \rho f([K^+]_o, [Na^+]_i)$ focusing on the “acceleration” term f which models the sensitivity to ion concentration changes, are warranted by the existence of a constant steady-state rate ρ , assumed to be voltage-independent. When V_m switches to $V_{dr} > -10 \text{ mV}$, dramatically shifted ΔV_m to large positive values impacts some of the binding and translocation steps in the kinetic model of the pump and questions the biophysical plausibility of keeping ρ constant. In particular, where the perturbing voltage transients like the electrographic seizure we used, produce a jump near V_{dr} *not resulting* from moderately elevated $[K^+]_o$, i.e., E_K not much above V_r , a large and lasting positive transient is produced. If further studies prove the bistability in V_m is electrophysiologically plausible, moving to a more detailed macroscopic model of the pump might be required with ρ explicitly depending on the full form of the electrochemical potential. For the pump rate ρ in units of molar flux, we can write [69]:

$$\rho \sim \Delta G + \Delta\tilde{\mu}_H \text{ (mM/s)}, \quad \text{where } \Delta\tilde{\mu}_H = \Delta\mu + zFV_m \text{ (RT units)},$$

$$RT \ln(c_{ext}/c_{in}) + zFV_m < -\Delta G, \quad \text{for active transport,} \quad (16)$$

where ΔG represents the purely chemical potential energy from ATP hydrolysis, and within the electrochemical part $\Delta\tilde{\mu}_H$ we recognize the Nernstian, or osmolar contribution $\Delta\mu = RT \ln(c_{ext}/c_{in})$ and the electrical part zFV_m that impacts ρ under prolonged depolarization at V_{dr} . An implicit assumption not typically discussed is that only near the nominal equilibrium V_r where the electrochemical gradient ΔV_m is small and the osmolar contribution large and steady, the FV_m term could be eventually neglected. The inequality in Eq. 16 is the typical condition for a sustained primary active transport, with sign convention in $-\Delta G$ representing the amount of free energy available from hydrolysis of a mole ATP, rather

⁵ We use the term in the context of the *catastrophe theory* of dynamical systems [65], [66] and *catastrophic bifurcations* [67], initially formulated over the impact of the same instability we observed - the fold bifurcation, on the global behavior of both, natural and man-made systems.

than the barrier height in the enzymatic reaction [71], [69]. Some variants of the macroscopic model of the pump have kept the voltage dependence [72] and have produced effects in whole-cell dynamics attributable to the Na-K pump. In such models, the eventual effects of voltage bistability could be directly tested. Stoichiometry coefficients have been omitted in Eq. 16 for simplicity.

The electrogenic sodium bicarbonate Na^+/HCO_3^- cotransporter (NBCe1) specifically implicated in glial metabolic and other functions, is another important candidate to be analyzed in the context of bistability since the reversal of the polarity of ΔV_m would cause switching of the transport direction and in turn the pH modulation of the cell between alkalization and acidification, and consequently of the immediate extracellular environment [7].

Of the other transporters potentially “vulnerable” to bistability let us mention the astrocytic GABA transporters (GAT1-GAT3) expressed in local cortical circuits [73], [74], modeled macroscopically as explicitly V_m dependent [75].

- **(I4), (S3) Switching between the two resting states may introduce erratic transients in trans-junctional voltage over the GJCs** – It has been shown that the conductance and rectification of GJCs are dependent on the trans-junctional voltage V_j between the connected cells across a wide range of the Connexin isoforms [76], [77], [78], and specifically for the Connexin43 hemichannels, one of the two most abundant subtypes assembling the astrocytic GJCs, with Connexin30 [79]. Due to the nonlinear steady-state I-V relationship and the nonlinear $g_{gjc}(V_j)$ in a wider V_j range in most GJCs [80], [81], the complex two-stage gating of the hemichannels may result in erratic behavior of the GJC if the connected cells are prone to switching between markedly separated V_r and V_{dr} . The notable difference between the *instantaneous and steady* $g_{gjc}(V_j)$ [77], introduces another major uncertainty in the eventual models [81]. The origin of such uncertainty between the residual and fully conductive conformations could be in principle justified by an atomic level model of GJC electrostatics [82] suggesting complex Coulombic profiles, potentially vulnerable to erratic voltage transients.
- **(I5), (S4) Glial encoding of $[K^+]_o$ variations as a signal gets a distinct state** – In the present understanding of the *encoding capability* of glial membrane, the glial V_m with certain low-pass filtering capability (with $\tau_m = C_{eff}/g_{slope} \approx 10ms$ for 20pF patch capacitance) close to linearly encodes $[K^+]_o$ variations as a signal through $(V_m - E_K)$. We can also say E_K itself smooth out the real-time K^+ variations from neuronal discharging partly due to the low-pass filtering of the ECS to volume transmission signals [57] and partly due to the $\log(c_{out}/c_{in})$ nature of Nernstian dependence. The emergence of V_{dr} introduces therefore a distinct, depolarized state potentially detectable on various timescales by a suitable measurement setup. In other words, V_r and V_{dr} encode (a) an almost linear potassium electrode, and (b) a deformed, N-shaped I-V relationship of deregulated conductance(s), respectively, Fig. 6A.

The presumed ion-homeostatic role of Kir4.1 in glia was not discussed in the context of bistability because the differential contributions of the different ion transport mechanisms are still elusive [83], and a reasonably reduced mathematical model addressing the spatial complexity of volume transmission in neuroglial circuits requires a dedicated experimental study for detecting the ranges of those parameters critical to the ion homeostatic effects.

In summary, the proposed minimal 2-dimensional model of the interplay between WR-Kir and K2P currents in astrocytic membrane shows that deregulations turning WR-Kir current into inwardly rectified, robustly produce a second very depolarized steady state of V_m and a whole-cell behavior considered markedly non-physiological within glial biology. To prove or refute such bistability as neurobiologically plausible, a measurement protocol well suited for transient V_m changes would be needed, probably employing voltage imaging, a dynamic (current) clamp, and cell assays displaying deregulated Kir4.1 or sufficient densities of Kir4.1/Kir5.1 channels of glial origin.

(U1) The proposed model, Eq. 13, is of general biophysical utility, directly applicable to the interplay between Kir and K2P currents in membranes of other systems where K2P channel variants display nonnegligible activation kinetics, like in the heart and kidneys, see [18] for more cases. Bistability showing comparable voltage separation of V_r and V_{dr} like presented has been already observed in cardiomyocytes in hypokalemic conditions [14], where strongly-rectifying Kir2.1 channels interwork with the linear K2P-TWIK channels.

Author contributions – PJ and LK designed the study. PJ formulated the models, did the parameter analysis, and wrote the paper. PJ and DS did the numerical simulations. PJ and LK assessed the results.

Declaration of Interests - The authors declare no competing interests.

Acknowledgments – We thank Prof. Christian Steinhäuser and Dr. Gerald Seifert for sharing with us the unique recordings from isolated astrocytes [12] of both Kir and K2P currents, for their lasting support in getting a sense of data and experimental limitations, as well as to CS on the numerous discussions and critical inputs. We thank Prof. Stephen Traynelis for warranting us to digitize and use the printed graphs from [9]. We thank Prof. Meyer Jackson for his comments on the model of I_{res} current, and for his inspiring treatment of biophysics of open pores [27] which motivated our modeling on several points. We thank Prof. Pavle Andjus for his comments on the simulation results. This study was partly funded by the National Institute of Mental Health (US), grant numbers MH117769 and MH125030 to PJ.

The XPPAUT .ode files for the bifurcation analysis and simulations will be available in *ModelDB* at <https://senselab.med.yale.edu/ModelDB>, under the model name “*Glial voltage dynamics driven by Kir & K2P currents*”.

Appendix-1 Short-pore model of WR-Kir channel and physiological Mg^{2+} block

We base our model of Kir current on (i) K^+ conduction through a *short pore* (Fig. A1), common to all K^+ channels - confined to the part of the transmembrane structure, consisting of a selectivity filter (SF) extending into the internal water-filled *central cavity* [84], [85] and on (ii) *physiological blocking* of the pore by cytoplasmic cations as a permeability modulation mechanism. Coulombic interactions within the short pore are therefore used to explain the permeation mechanisms as an interaction between the blocking Mg^{2+} and permeant K^+ ions, as a basis for a weak rectification. Unlike in strong inward rectification, where both, the internal Mg^{2+} and/or polyamines fully block outward flux [34], [86], in the outward permeation scenario of a weakly rectifying pore (Fig. A1C) the partial and flickering block allows the entrance of permeant ions into the SF and modulates their electrodiffusion at high rates. This pore model is crucial for explaining the *anomalous*, inward rectification of Kir conductances, which can't be described by Nernst-Planck (NP) formalism based on electrochemical gradients over open, leaky channels. The short pore model applied to outward conduction in WR-Kir channels, allows extending the NP model with a non-constant field and in turn a voltage-dependent permeability, equation (9), under the assumptions of a changing Coulombic profile with voltage. These extensions formulate the main assumptions of the I_{res} model [27].

In line with the above assumptions, recent evidence from single-channel recordings and molecular dynamics simulations of the potassium KcsA pore [87] suggests that the voltage and ligands induce *structural fluctuation* changes within the electrostatics, Coulombic profile of SF which produces a universal pseudo-gating of an open pore at SF, *without* introducing a conformational change and gating.

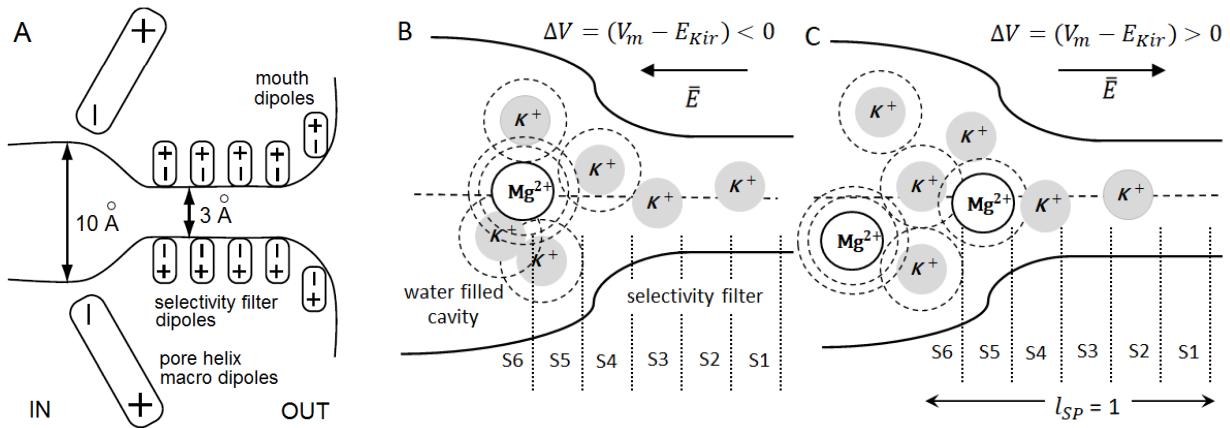


Figure A1 - Short pore model of permeation through generic weakly-rectifying Kir channels – (A) A *short-pore* view of the Kir pore consisting of a selectivity filter (SF) and the inner, water-filled *central cavity*. The sketch shows the sources of electrostatic interaction along with the transmembrane structure acting on permeant and blocking ions, modified from [88]. Inside the SF, selectivity filter dipoles create binding sites (S1 to S4), corresponding to energy wells where permeant ions are stabilized between the transitions. **(B)** and **(C)**, A simplified one-dimensional view of the short pore showing the different voltage dependence of the Mg^{2+} block and the Coulombic interaction with the permeant ions. From negative to positive $\Delta V_m = (V_m - E_{Kir})$, and constant or slowly varying $[K^+]_o$, the resulting force on Mg^{2+} and K^+ ions changes and the resulting blocking events are qualitatively different, see text for details. Arrows show the direction of the electrical field \bar{E} on a positive ion along the reaction coordinate. We assign a unitary length l_{SP} (shown in C) to the extent of the pore over which we model potential energy landscape. Dashed circles around the ions in (B) and (C) represent the full or partial hydration shells. The length of the SF without the outer vestibule in (B) and (C) is disproportionately shorter than in (A), to keep the image compact.

The short-pore model assumes the concentration of Mg^{2+} and K^+ within the central cavity and at the external pore vestibule, correspond to the physiological intracellular and extracellular bath concentrations respectively. Local, *relative, nonequilibrium concentration changes* due to effects like the attraction of cations by rings of negatively charged residues, in vestibules on either side of the SF entrance, are neglected.

To describe both, the inward and outward permeation, we assume that the transmembrane voltage V_m drops over the whole *short pore* - over the whole cavity and the SF, but the fraction δ introduced in Eq. 7 reduces it to $\delta\Delta V_m$ influencing with a smaller fraction the middle of the pore and S5 position where the outward barrier is centered, as marked in Fig. 3B. For completeness, the S0 position (not shown in Fig. A1B and A1C) would be just outside the SF, in the outer vestibule. This is a similar approach to the one used in permeation studies of weak rectification in renal Kir1.1 / ROMK1 [89, 90]. This pore model suggests that the blocking cation moves between two *modulatory* sites [91] depending on ΔV_m polarity, thereby defining the main rectification barrier(s).

Inward pseudo gating - For negative and very small positive net driving forces ΔV_m , (Fig. A1B), the resulting electrostatics from pore helix macro dipoles keeps blocking Mg^{2+} ions within the cavity (designated by position S6), so that the inward rectification results from a competition of permeant K^+ and Mg^{2+} ions for the central, axial positions within the cavity. Even though ΔV_m influences S6 position with a much smaller fraction, not exceeding $\delta\Delta V_m$ (Fig. 3) the dependence of inward flux on V_m for $\Delta V_m < 0$ is still exerted on the K^+ ion in S6 through the multi-ion file within SF (binding positions S1 to S4), which contributes to the resulting Coulombic forces and ion-crowding within the central cavity (represented by S5 and S6 positions). By resulting force, in this simplified view, we mean Coulombic repulsion between the permeant ions acting in parallel to the stabilizing attractive force on them coming from the negative end of pore helix macro dipoles (Fig. A1A), tilted so to make the center of the cavity electrostatically favorable point for a cation [26]. Hagiwara's model of the macroscopic inwardly rectified Kir currents assumes the existence of equilibrium pore-open probabilities of inward permeation suggesting a Boltzmann term in Eq. 3 for describing the macroscopic conductance (rather than barrier crossing rates), analogous to the open and closed probabilities in gated ion channels, see [34] for Kir-specific review.

Outward pseudo gating - In the reverse case, for a more positive driving force $V_m > -50mV$ (Fig. A1C), an outwardly directed net driving force acts on permeant and blocking cations, pushing partly or fully dehydrated Mg^{2+} ion towards the entry of the SF, which results in a partial flickering plug of the pore at the S5 site. Blocking ion at S5 in conjunction with the hydrophobic repulsion at SF entry creates an ion association or entry barrier to the permeant K^+ ion, 2λ wide in units of fractional electrical distance, Fig 3B, extending through S4 and S3 positions, Fig. A1C.

The different nature of the resulting electrostatics in these two cases implicates different permeation mechanisms and warrants the use of a different biophysical description of unidirectional fluxes. We, therefore, model the unidirectional fluxes as additive over the whole V_m range of the measured Kir4.1 current. In other words, the proposed modeling approach suggests *that in its structure-function a weak rectifier results as a superposition of inward and outward rectifiers*. Single mutation studies [22], [92] suggested their structural determinants are very similar, whereas a single point mutation flips the pore from a strong Kir2.1 to a weak Kir1.1 rectifier.

Appendix-2

Table 2 - Experimental studies reporting altered properties of Kir4.1 current

Altered current	Exp. model, Reference	WR-Kir inward	WR-Kir outward	Cell type	Comment
Kir4.1 current	Astrocytes in ALS [49]	↓↓	↓↓	Astrocytes in culture	Non-Kir outward current increased markedly in the ALS model
Kir4.1 outward current	Astrocytes in Huntington's Disease [48]	↓	↓↓↓	Astrocytes in slices	
Currents through heteromeric Kir4.1/Kr5.1 channels	[45]	Not altered	Abolished	HEK-293 cells	Kir channels introduced by DNA transfection
Kir4.1 current	Astrocytes in Depression [93]	↑↑	↑↑↑	Astrocytes in slices	Not considered in the parametric analysis since the I-V curve remains monotonic.

Table 2 – Selection of studies where quantitative alteration of the macroscopic Kir current in electrophysiological recordings has been reported, and some form of identification of weakly rectified Kir4.1 or inwardly rectified Kir4.1/Kir5.1 has been elaborated. Many more disease models have reported some *association* of model phenotypes to Kir channels in astrocytes, but differential quantitation of the macroscopic currents or conductances on a single cell has not been among the study objectives.

References

1. Zhou, M., Y. Du, S. Aten, and D. Terman, On the electrical passivity of astrocyte potassium conductance. *J Neurophysiol*, 2021. **126**(4): p. 1403-1419.
2. Kuffler, S., J.G. Nicholls, and R. Orkand, Physiological properties of glial cells in the central nervous system of amphibia. *J Neurophysiol*, 1966. **26**: p. 768-787.
3. Kettenmann, H. and C. Steinhäuser, *Receptors for neurotransmitters and hormones*, in *Neuroglia*, H. Kettenmann, and Ransom, BR., Editor. 2005, Oxford University Press: New York. p. 131-145.
4. Verkhratsky, A. and M. Nedergaard, Physiology of Astroglia. *Physiol Rev*, 2018. **98**(1): p. 239-389.
5. Bedner, P., R. Jabs, and C. Steinhäuser, Properties of human astrocytes and NG2 glia. *Glia*, 2019. **68**: p. 756-767.
6. Kettenmann, H., K.H. Backus, and M. Schachner, Aspartate, glutamate and γ -aminobutyric acid depolarize cultured astrocytes. *Neuroscience Letters*, 1984. **52**: p. 25-29.
7. Ransom, B.R., Glial modulation of neural excitability mediated by extracellular pH: a hypothesis revisited. *Prog Brain Res*, 2000. **125**: p. 217-28.
8. Henneberger, C. and D. Rusakov, Monitoring local synaptic activity with astrocytic patch pipettes. *Nature Protocols*, 2012. **7**: p. 2171-2179.
9. Traynelis, S.F. and R. Dingledine, Potassium-induced spontaneous electrographic seizures in the rat hippocampal slice. *J Neurophysiol*, 1988. **59**(1): p. 259-76.
10. Ballanyi, K., P. Grafe, and G. ten Bruggencate, Ion activities and potassium uptake mechanisms of glial cells in guinea-pig olfactory cortex slices. *J. Physiol*, 1987. **328**: p. 159-174.
11. Somjen, G.G., *Ions in the brain: normal function, seizures, and stroke*. 2004, Oxford; New York: Oxford University Press. xxix, 470 p.
12. Seifert, G., K. Hüttmann, D.K. Binder, C. Hartmann, A. Wyczynski, et al., Analysis of Astroglial K⁺ Channel Expression in the Developing Hippocampus Reveals a Predominant Role of the Kir4.1 Subunit. *J. Neurosci.*, 2009. **29**: p. 7474-7488.
13. Steinhäuser, C., Seifert, G., Deitmer, J.W., *Physiology of astrocytes: ionchannels and ion transporters*, in *Neuroglia*. 2013, Oxford University Press. p. 185–196.
14. Zuo, D., Chen, K., Zhou, M., Liu, Z., Chen, H, Kir2.1 and K2P1 channels reconstitute two levels of resting membrane potential in cardiomyocytes. *J Physiol*, 2017. **595**: p. 5129–5142.
15. Herrera-Perez, S., A. Campos-Rios, L. Rueda-Ruzafa, and J.A. Lamas, Contribution of K2P Potassium Channels to Cardiac Physiology and Pathophysiology. *Int J Mol Sci*, 2021. **22**(12).
16. Hebert, S., Desir, G., Giebisch, G., Wang, W., Molecular Diversity and Regulation of Renal Potassium Channels. *Physiol Rev*, 2005. **85**: p. 319 –371.
17. Welling, P., Roles and Regulation of Renal K Channels. *Ann Rev Physiol*, 2016. **78**: p. 415-435.
18. Sepúlveda, F.V., Cid, L.P., Teulon, J., Niemeyer, M.I., Molecular Aspects of Structure, Gating, and Physiology of pH-Sensitive Background K2P and Kir K-Transport Channels. *Physiol Rev*, 2015: p. 95:179–217.
19. Izhikevich, E.M., *Dynamical Systems in Neuroscience - The Geometry of Excitability and Bursting*. 2007, Cambridge, Massachusetts: The MIT Press.
20. Gonzalez, C., D. Baez-Nieto, I. Valencia, I. Oyarzun, P. Rojas, et al., K(+) channels: function-structural overview. *Compr Physiol*, 2012. **2**(3): p. 2087-149.
21. Hagiwara, S. and K. Takahashi, The Anomalous Rectification and Cation Selectivity of the Membrane of a Starfish Egg Cell. *J. Membrane Biol.*, 1974. **18**: p. 61-80.
22. Wible, B., M. Tagliatela, E. Ficker, and A.M. Brown, Gating of inwardly rectifying K⁺ channels localized to a single negatively charged residue. *Nature*, 1994: p. 371:246.

23. Kurata, H.T., M. Rapedius, M.J. Kleinman, T. Baukrowitz, and C.G. Nichols, Voltage-dependent gating in a "voltage sensor-less" ion channel. *PLoS Biol*, 2010. **8**(2): p. e1000315.
24. Ohmori, H., Inactivation kinetics and steady-state current noise in the anomalous rectifier of tunicate egg cell membranes. *J.Physiol.*, 1978: p. 281:77–99.
25. Kubo, Y., T.J. Baldwin, Y.N. Jan, and L.Y. Jan, Primary structure and functional expression of a mouse inward rectifier potassium channel. *Nature*, 1993: p. 362:127-133.
26. Hille, B., *Ionic Channels of Excitable Membranes, 3rd Ed.* 2001, Sunderland, MA: Sinauer Associates Inc.
27. Jackson, M.B., *Molecular and Cellular Biophysics.* 2006, New York: Cambridge Univ. Press.
28. Schewe, M., E. Nematian-Ardestani, H. Sun, M. Musinszki, S. Cordeiro, et al., A non-canonical voltage-sensing mechanism controls gating in K2p K⁺ channels. *Cell*, 2016. **164**: p. 937–949.
29. Meeks, J.P. and S. Mennerick, Astrocyte membrane responses and potassium accumulation during neuronal activity. *Hippocampus*, 2007. **17**(11): p. 1100-8.
30. Edvinsson, J., Shah, A.J., Palmer, L.G., Kir4.1 K⁺ channels are regulated by external cations. *Channels (Austin)*, 2011: p. 5(3):269-279.
31. Marcus, R., Chemical and Electrochemical Electron-Transfer Theory. *Annu. Rev. Phys. Chem.*, 1964. **15**: p. 155-196.
32. Matyushov, D.V., Protein electron transfer: is biology thermodynamic? *J Phys Condens Matter*, 2015. **27**(47): p. 473001.
33. Peters, B., Common features of extraordinary rate theories. *J Phys Chem B*, 2015. **119**(21): p. 6349-56.
34. Lu, Z., Mechanism of Rectification in Inward-Rectifier K⁺ Channels. *Annual Rev Physiol*, 2004: p. 66:103-129.
35. Borg-Graham, L., *Interpretations of Data and Mechanisms for Hippocampal Pyramidal Cell Models*, in *Cerebral Cortex - Models of Cortical Circuits.* 1999, Springer Science: New York. p. 19-137.
36. Zhou M., G. Xu, M. Xie, X. Zhang, G.P. Schools, et al., TWIK-1 and TREK-1 are potassium channels contributing significantly to astrocyte passive conductance in rat hippocampal slices. *J Neurosci*, 2009. **29**: p. 8551-8564.
37. Chen, H., Zuo, D., Zhang, J., Zhou, M., Ma, L., Classification of 2-pore domain potassium channels based on rectification under quasi-physiological ionic conditions. *Channels*, 2014. **8**: p. 503-508.
38. Ransom, B.R. and S. Goldring, Ionic determinants of membrane potential of cells presumed to be glia in cerebral cortex of cat. *J Neurophysiol*, 1973. **36**(5): p. 855-68.
39. Honore, E., The neuronal background K2P channels - focus on TREK1. *Nat. Rev. Neurosci.*, 2007. **8**: p. 251-261.
40. Enyedi, P. and G. Czirjak, Molecular background of leak K⁺ currents: two-pore domain potassium channels. *Physiol Rev*, 2010. **90**(2): p. 559-605.
41. Eisenman, G., Horn, R., Ionic selectivity revisited: The role of kinetic and equilibrium processes in ion permeation through channels. *J Membrane Biol*, 1983. **76**(3): p. 197–225.
42. Johnston, D. and S.M.-S. Wu, *Foundations of Cellular Neurophysiology.* 1995, Cambridge, Massachusetts: The MIT Press.
43. Hodgkin, A.L. and P. Horowicz, The influence of potassium and chloride ions on the membrane potential of single muscle fibres. *J. Physiol*, 1959. **148**: p. 127-160.
44. Destexhe, A., Huguenrad, J., Nonlinear Thermodynamic Models of Voltage-Dependent Currents. *J Comp Neurosci*, 2000. **9**: p. 259–270.
45. Marmolejo-Murillo, L.G., I.A. Arechiga-Figueroa, E.G. Moreno-Galindo, T. Ferrer, R. Zamora-Cardenas, et al., Kir4.1/Kir5.1 channels possess strong intrinsic inward rectification determined by a voltage-dependent K⁺-flux gating mechanism. *J Gen Physiol*, 2021. **153**(5).

46. Doedel, E., A.R. Champneys, T.F. Fairgrieve, Y.A. Kuznetsov, B. Sandstede, et al. AUTO 97: Continuation and bifurcation software for ordinary differential equations (with HomCont). 1997. indy.cs.concordia.ca.
47. Ermentrout, B., *Simulating, analyzing, and animating dynamical systems: a guide to XPPAUT for researchers and students*. 2002, Philadelphia: Society of Industrial and Applied Mathematics (SIAM).
48. Tong, X.e.a., Astrocyte Kir4.1 ion channel deficits contribute to neuronal dysfunction in Huntington's disease model mice. *Nat. Neurosci.*, 2014: p. 17:694.
49. Bataveljić, D., Nikolić L., Milošević M., Todorović N., Anđus P.R., Changes in the astrocytic aquaporin-4 and inwardly rectifying potassium channel expression in the brain of the amyotrophic lateral sclerosis SOD1(G93A) rat model. *Glia*, 2012. **60**(12): p. 1991–2003.
50. Hibino, H., A. Inanobe, K. Furutani, S. Murakami, I. Findlay, et al., Inwardly rectifying potassium channels: their structure, function, and physiological roles. *Physiol Rev*, 2010. **90**(1): p. 291-366.
51. Hibino, H., A. Fujita, K. Iwai, M. Yamada, and Y. Kurachi, Differential assembly of inwardly rectifying K⁺ channel subunits, Kir4.1 and Kir5.1, in brain astrocytes. *J Biol Chem*, 2004. **279**(42): p. 44065-73.
52. Soe, R., M. Andreasen, and D.A. Klaerke, Modulation of Kir4.1 and Kir4.1-Kir5.1 channels by extracellular cations. *Biochim Biophys Acta*, 2009. **1788**(9): p. 1706-13.
53. Barreto, E. and J. Cressman, Ion concentration dynamics as a mechanism for neuronal bursting. *J Biol Phys*, 2011. **37**: p. 361–373.
54. Seifert, G., C. Henneberger, and C. Steinhäuser, Diversity of astrocyte potassium channels - An update. *Brain Res Rev*, 2018. **126**: p. 26-36.
55. Izhikevich, E.M., Which model to use for cortical spiking neurons? *IEEE Trans Neural Networks*, 2004. **15**(5): p. 1063 - 1070.
56. Benbow, S.J. *Graph Grabber*. 2020. Quintessa, Henley-on-Thames, United Kingdom.
57. Bedard, C., H. Kroger, and A. Destexhe, Model of low-pass filtering of local field potentials in brain tissue. *Physical Review E*, 2006. **73**(5).
58. Tyson, J.J., R. Albert, A. Goldbeter, P. Ruoff, and J. Sible, Biological switches and clocks. *J R Soc Interface*, 2008. **5 Suppl 1**: p. S1-8.
59. Gallaher, J., M. Bier, and J.S. van Heukelum, First order phase transition and hysteresis in a cell's maintenance of the membrane potential--An essential role for the inward potassium rectifiers. *Biosystems*, 2010. **101**(3): p. 149-55.
60. Ciani, S., Krasne, S., Miyazaki, S., Hagiwara, S., A model for anomalous rectification: electrochemical-potential-dependent gating of membrane channels. *J. Membrane Biol*, 1978. **44**: p. 103-134.
61. Cressman, J., Ullah, G., Ziburkus, J., Schiff, S.J., Barreto, E., The influence of sodium and potassium dynamics on excitability, seizures, and the stability of persistent states: I. Single neuron dynamics. *J Comput Neurosci*, 2009. **26**: p. 159–170.
62. Krishnan, G.P., G. Filatov, A. Shilnikov, and M. Bazhenov, Electrogenic properties of the Na⁽⁺⁾/K⁽⁺⁾ ATPase control transitions between normal and pathological brain states. *J Neurophysiol*, 2015. **113**(9): p. 3356-74.
63. Erhardt, A.H., K.A. Mardal, and J.E. Schreiner, Dynamics of a neuron-glia system: the occurrence of seizures and the influence of electroconvulsive stimuli : A mathematical and numerical study. *J Comput Neurosci*, 2020. **48**(2): p. 229-251.
64. Ma, B., Buckalew, R., Du, Y., Kiyoshi, C.M., Alford, C.C., Wang, W., McTigue, D.M., Enyeart J.J., Terman D., Zhou M., Gap junction coupling confers isopotentiality on astrocyte syncytium. *Glia*, 2016. **64**: p. 214-226.
65. Gilmore, R., *Catastrophe theory for scientists and engineers*. 1993, New York: Dover Publications. xvii, 666 p.
66. Zeeman, E.C., *Catastrophe theory : selected papers, 1972-1977*. 1977, Reading, Mass.: Addison-Wesley Pub. Co., Advanced Book Program. x, 675 p.

67. Abraham, R. and C.D. Shaw, *Dynamics-the geometry of behavior - Part Four: Bifurcation Behavior*. The Visual mathematics library Vismath books. 1982, Santa Cruz, Calif.: Aerial Press.
68. De Weer, P., D.C. Gadsby, and R.F. Rakowski, Voltage dependence of the Na-K pump. *Annu Rev Physiol*, 1988. **50**: p. 225-41.
69. Läuger, P., Thermodynamic and kinetic properties of electrogenic ion pumps. *Biochem Biophys Acta*, 1984. **779**: p. 307-341.
70. Poulsen, H., P. Morth, J. Egebjerg, and P. Nissen, Phosphorylation of the Na⁺,K⁺-ATPase and the H⁺,K⁺-ATPase. *FEBS Lett*, 2010. **584**(12): p. 2589-95.
71. Adam, G., Läuger, P., and Stark, G., *Physikalische Chemie und Biophysik*. 2009: Springer-Verlag. 619.
72. Forrest, M.D., The sodium-potassium pump is an information processing element in brain computation. *Front Physiol*, 2014. **5**: p. 472.
73. Fattorini, G., M. Melone, and F. Conti, A Reappraisal of GAT-1 Localization in Neocortex. *Front Cell Neurosci*, 2020. **14**: p. 9.
74. Zafar, S. and I. Jabeen, Structure, Function, and Modulation of gamma-Aminobutyric Acid Transporter 1 (GAT1) in Neurological Disorders: A Pharmacoinformatic Prospective. *Front Chem*, 2018. **6**: p. 397.
75. Hoshino, O., R. Kameno, J. Kubo, and K. Watanabe, Spatiotemporal regulation of GABA concentration in extracellular space by gliotransmission crucial for extrasynaptic receptor-mediated improvement of sensory tuning performance in schizophrenia. *J Comput Neurosci*, 2020. **48**(3): p. 317-332.
76. Bargiello, T.A., S. Oh, Q. Tang, N.K. Bargiello, T.L. Dowd, et al., Gating of Connexin Channels by transjunctional-voltage: Conformations and models of open and closed states. *Biochim. Biophys. Acta*, 2018. **1860**: p. 22–39.
77. Oh, S., and Bargiello, T., Voltage Regulation of Connexin Channel Conductance. *Yonsei Med J*, 2015. **56**: p. 1-15.
78. Maciunas, K., M. Snipas, N. Paulauskas, and F.F. Bukauskas, Reverberation of excitation in neuronal networks interconnected through voltage-gated gap junction channels. *J Gen Physiol*, 2016. **147**(3): p. 273-88.
79. Bukauskas, F.F., A. Bukauskiene, and V.K. Verselis, Conductance and permeability of the residual state of connexin43 gap junction channels. *J Gen Physiol*, 2002. **119**(2): p. 171-85.
80. Baigent, S., J. Stark, and A. Warner, Modelling the Effect of Gap Junction Nonlinearities in Systems of Coupled Cells. *J Theor Biol*, 1997. **186**: p. 223-239.
81. Baigent, S., Cells coupled by voltage-dependent gap junctions: the asymptotic dynamical limit. *Biosystems*, 2003. **68**(2-3): p. 213-22.
82. Escalona, Y., J.A. Garate, R. Araya-Secchi, T. Huynh, R. Zhou, et al., Exploring the Membrane Potential of Simple Dual-Membrane Systems as Models for Gap-Junction Channels. *Biophys J*, 2016. **110**(12): p. 2678-2688.
83. MacAulay, N., Molecular mechanisms of K⁺ clearance and extracellular space shrinkage-Glia cells as the stars. *Glia*, 2020. **68**(11): p. 2192-2211.
84. Doyle, D.A., J. Morais Cabral, R.A. Pfuetzner, A. Kuo, J.M. Gulbis, et al., The Structure of the Potassium Channel: Molecular Basis of K⁺ Conduction and Selectivity. *Nature*, 1998. **280**: p. 69-77.
85. Allen, T.W., A. Bliznyuk, A.P. Rendell, S. Kuyucak, and S.-H. Chung, The potassium channel: Structure, selectivity and diffusion. *J Chem Phys*, 2000. **112**: p. 8191-8204.
86. Matsuda, H., Effects of external and internal K⁺ ions on magnesium block of inwardly rectifying K⁺ channels in guinea-pig heart cells. *J. Physiol*, 1991: p. 435:83.
87. Heer, T.H., Posson, D.J., Wojtas-Niziuski, W., Nimigeon, C.M., Bernèche, S., Mechanism of activation at the selectivity filter of the KcsA K⁺ channel. *eLife*, 2017: p. 6:e25844.
88. Chung, S.H., T.W. Allen, M. Hoyle, and S. Kuyucak, Permeation of ions across the potassium channel: Brownian dynamics studies. *Biophys J*, 1999. **77**(5): p. 2517-33.

89. Yang, L., J. Edvinsson, H. Sackin, and L. Palmer, Interactions of external K⁺ and internal blockers in a weak inward-rectifier K⁺ channel. *J Gen Physiol* 2012b: p. 140:529.
90. Yang, L., J. Edvinsson, H. Sackin, and L.G. Palmer, Ion selectivity and current saturation in inward-rectifier K⁺ channels. *J.Gen.Physiol.*, 2012a: p. 139:145.
91. Hille, B., Schwartz, W, Potassium Channels as Multi-Ion Single-file Pores. *J Gen Physiol*, 1978. **72**: p. 409-442.
92. Lu Z., M., R., Electrostatic tuning of Mg²⁺ affinity in an inward-rectifier K⁺ channel. *Nature*, 1994: p. 371:243-245.
93. Cui, Y., Yang, Y., Ni, Z., Dong, Y., Cai, G., Foncelle, A., Ma, S., Sang, K., Tang, S., Li, Y., Shen, Y., Berry, H., Wu, S., Hu, H., Astroglial Kir4.1 in the lateral habenula drives neuronal bursts in depression. *Nature*, 2018. **554**: p. 323–327.